Supporting Information

Cobalt-Yttria Heterointerface on Nitrogen and Sulfur-Doped Carbon as a Durable Electrocatalyst for Metal-Air Battery and Overall Water Electrolysis

Parvathi Vijayakumar Geetha,[a] Anook Nazer Eledath[a] and Azhagumuthu Muthukrishnan[a,*]

[a] School of Chemistry, Indian Institute of Science Education and Research Thiruvananthapuram, Maruthamala P.O., Vithura 695551, Kerala, India

Email: muthukrishnan@iisertvm.ac.in

Kinetic Current Calculation

For oxygen reduction reaction

$$j_k(E) = \frac{j_D\,(E)\,j_{DL}}{j_{DL} - j_D(E)}$$

where,

$j_{\mathrm{k}}(E)$ = kinetic current

j_{DL} = limiting disk current (taken at 0.4 V vs. RHE for all catalysts)

$j_{\mathrm{D}}(E)$ = disk current (taken at 0.8 V vs. RHE for all catalysts and 0.9 V vs. RHE for Pt/C)

ECSA calculation

$$\mathrm{ECSA} = \frac{\mathrm{C}_{dl}}{\mathrm{C}_s}$$

where,

C_{dl} is the double-layer capacitance of the system, determined from the slope of linear fits to the graph of current (averaged from cathodic and anodic charging currents measured at 1.05 V vs. RHE) vs. scan rate.

$\mathrm{C_s}$ is the specific capacitance of the electrode; a typical value of 0.04 mF $\mathrm{cm^{-2}}$ is taken in alkaline solutions. [S1, S2]

Mass-specific and area-specific Δ*E* calculations

The kinetic current per real surface area can be calculated using the electrochemical surface area (ECSA) of the coated electrode as shown below

$$i_k(\mu A\ cm^{-2}_{\mathrm{ECSA}}) = \frac{I_k\ (\mu A)}{ECSA\ (cm^2)}$$

Similarly, the mass-specific kinetic current density can be calculated from the equation as given below

$$i_k(A\ g^{-1}) = \frac{I_k(A)}{W\ (g)}$$

Here, the amount of catalyst coated was 4.95 μg_{pt} for Pt/C and 99 µg for other catalysts.

The OER kinetic current densities were estimated assuming that the onset region is purely under kinetic control. Unlike ORR, the OER LSV does not exhibit a well-defined diffusion-limited region; therefore, the Koutecký-Levich (K-L) equation cannot be applied to determine the kinetic current. However, we make sure that the reaction is kinetically controlled using the rotational speed study. And here, the amount of catalyst coated was 99 µg for RuO_2 and other catalysts.

Therefore, to evaluate the catalytic performance, we fixed 10 A g^{-1}, and 10 $\mu A\ cm^{-2}_{ECSA}$, as the reference current density for mass-specific and area-specific ΔE calculations for both ORR and OER. The potential difference (ΔE) was determined from the difference between the potentials required to reach 10 A g^{-1} (mass-specific current density) and 10 10 $\mu A\ cm^{-2}_{ECSA}$ (area-specific current density**)** for the OER and ORR, respectively

TOF calculation

Turn over frequency (TOF): The TOF of the materials are calculated as previously reported procedure based on the following formula,[S3]

$$TOF = \frac{J \times N_A}{n \times F \times \tau}$$

where J is the current density at a fixed potential, N_A is the Avogadro number, and n is the number of electrons transferred (n is taken as 2 for HER and 4 for OER), F is the Faraday constant (96485 C mol^{-1}), and τ is the number of active sites involved in the reaction, which can be calculated using the following relation.

$$\tau = \frac{\text{area of CV curve}}{\text{scan rate} \times 1.601 \times 10^{-1}}$$

The area of the CV was estimated at a scan rate of 0.04 V s^{-1} in the non-faradaic region of the voltammogram.

Specific Capacity measurement

he specific capacity of the zinc-air battery was calculated based on the total discharge time and the mass of consumed zinc, using the relation:

$$\text{Specific Capacity} = \frac{I \times t}{W_{Zn}}$$

I- Current passed, t- Service hours, W_{Zn} - Zinc consumed

W_{Zn} = Initial weight of Zinc plate – Final weight of Zinc plate

Synthesis of $YCoO_3$

Yttrium cobalt oxide with the perovskite structure was synthesised by a high-energy dry ball-milling strategy using a Retsch PM 100 Planetary Ball Mill. The 1:1 mixture of yttria and cobalt oxide powder was placed in one-third of the SS jar volume. Another one-third of the jar was filled with stainless-steel 3 mm diameter balls, and the jar was sealed tightly. The mixer was ball-milled at 500 rpm for 12 h. Further, the ball-milled sample was pyrolysed in air at 900 ℃ for 5 h to obtain yttrium cobalt oxide with the perovskite structure.

Synthesis of Graphene oxide (GO)

Graphene oxide (GO) was synthesised through the oxidation of graphite with a modified Hummers Method.[S4] Concisely, 2 g each of $NaNO_3$ and graphite powder were introduced to 90 mL of concentrated H_2SO_4 in an ice bath, and the mixture was stirred for 4 hours. 12 g of $KMnO_4$ was added to the mixture, maintaining the temperature below 15 °C. The components were diluted with 184 mL of distilled water and stirred at 35 °C for 2 hours. The mixture was then refluxed at 98 °C for 15 minutes and subsequently cooled to room temperature. 40 mL of H_2O_2 was added to eliminate unreacted $KMnO_4$, followed by centrifugation and repeated washing with 0.1 M HCl and DIW. The resulting black residue was vacuum-dried at 60 °C for 8 hours to yield GO powder.

Preparation of PVA gel for solid-state ZAB

PVA gel was prepared using the previously reported procedure.[S5] Briefly, 2 g PVA was dispersed in 20 mL of DIW, and the mixture was refluxed at 90°C for 1.5 hours while being vigorously stirred. The aforementioned dispersion was mixed with 2 mL of 18 M KOH and 0.02 M zinc acetate solution, then added dropwise to obtain a transparent solution, which was then agitated for 30 minutes. After 12 hours of freezing, the finished gel was thawed at normal temperature. To improve its ionic conductivity, it was submerged in a solution of 0.2 M zinc acetate and 6 M KOH.

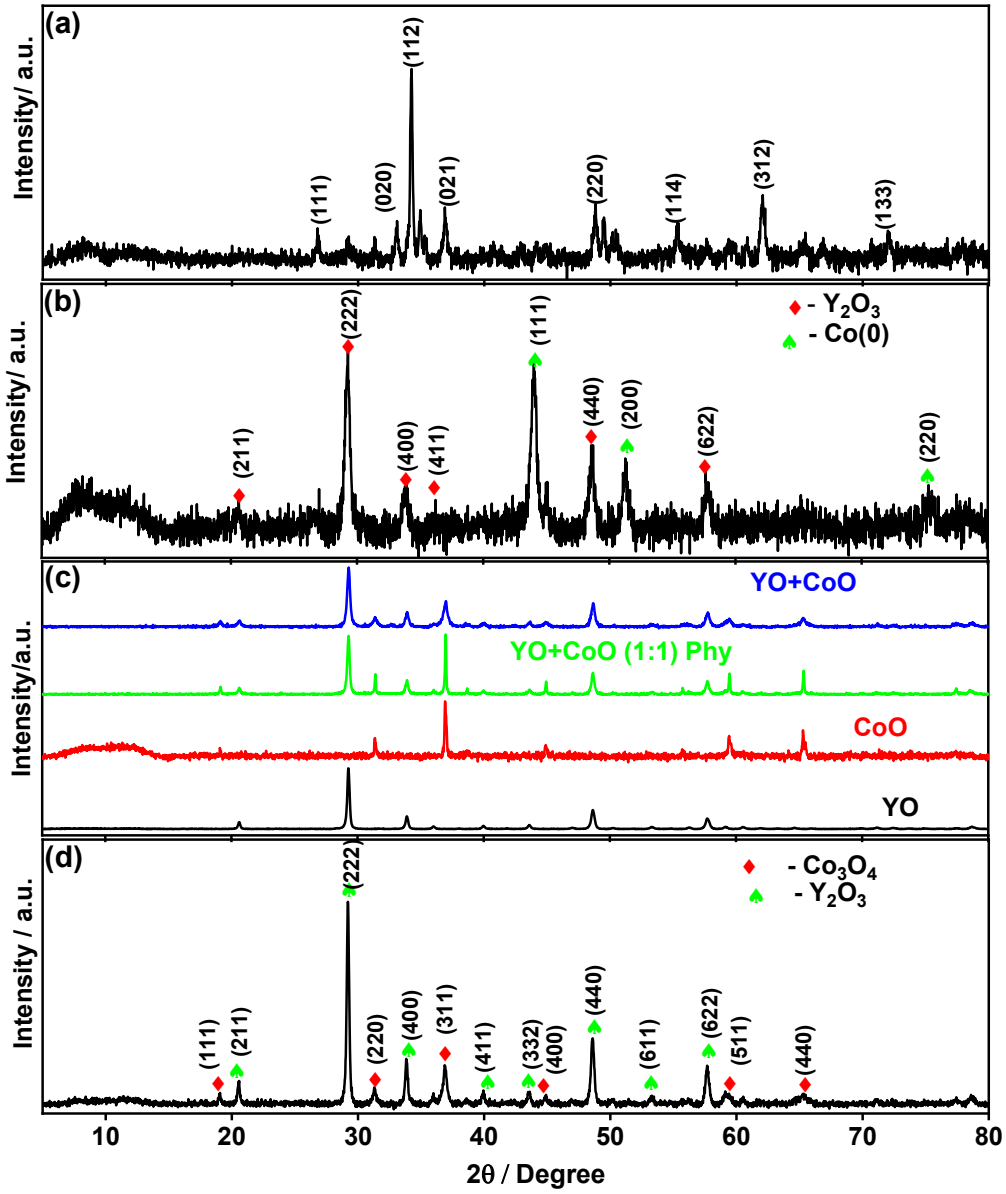

Figure S1. Powder XRD patterns of (a) $YCoO_3$, (b) heteroatoms-doped $YCoO_3$ ($YCoO_3$/N&S-rGO), (c) individual and physically mixed Y_2O_3 and Co_3O_4 and (d) YCO.

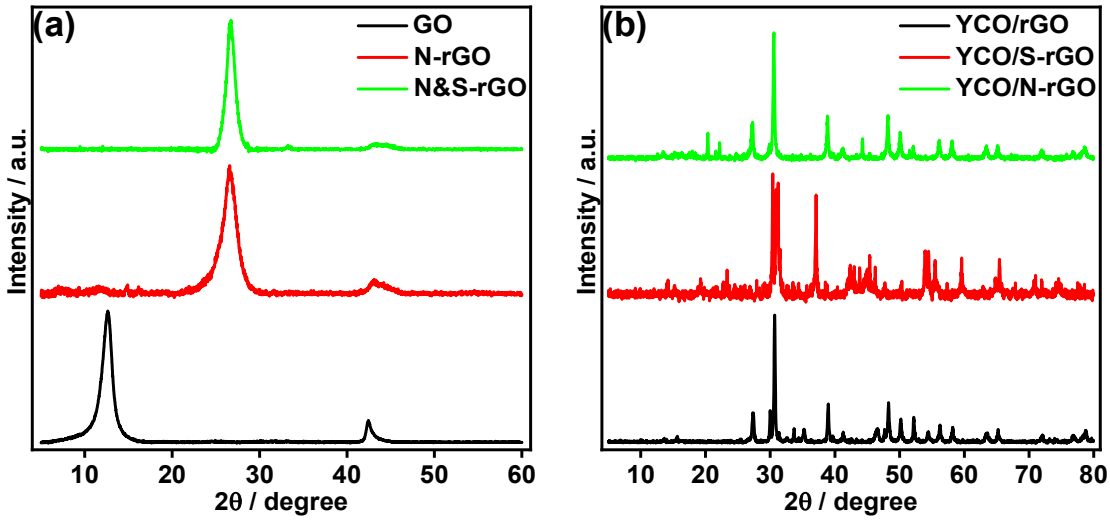

Figure S2. The powder XRD recorded for the control samples (a) undoped and heteroatom-doped carbon materials, and (b) YCO with heteroatom-doped carbon materials.

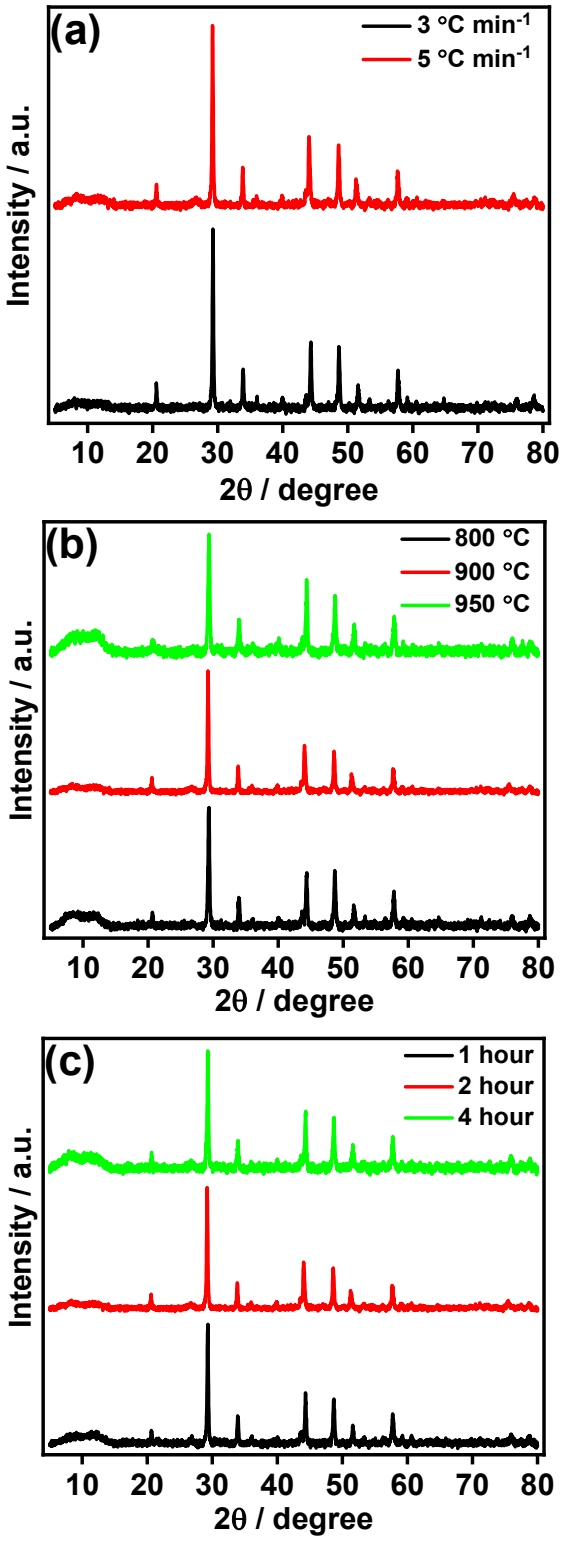

Figure S3. XRD patterns of YCO/N&S-rGO obtained from various parameter optimizations (a) at different ramp rates, (b) at different temperatures, and (c) at different dwelling time, of heat treatment in the N_2 atmosphere.

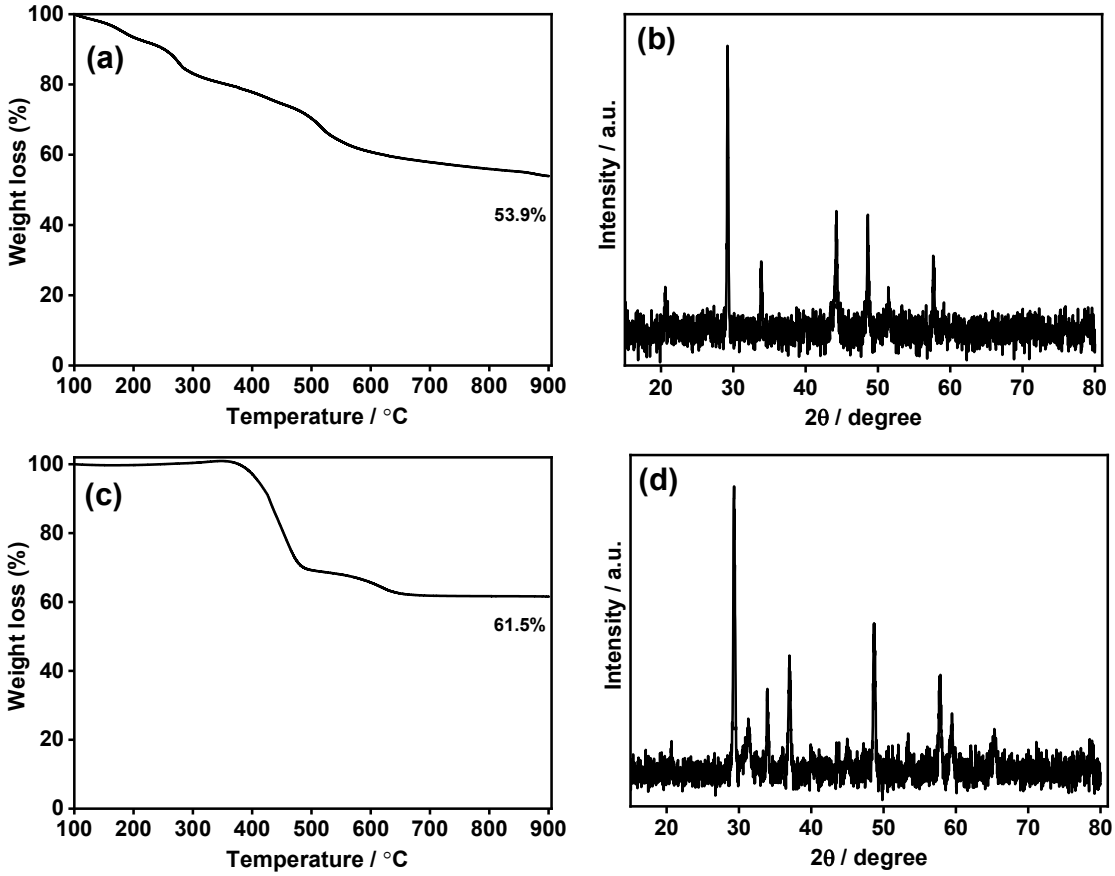

Figure S4. Thermogravimetric analysis of (a) YCO/N&S-GO precursors in N_2 atmosphere and (c)YCO/N&S-rGO in air atmosphere, (b) and (d) PXRD taken after the TGA analysis of (a) and (c), respectively.

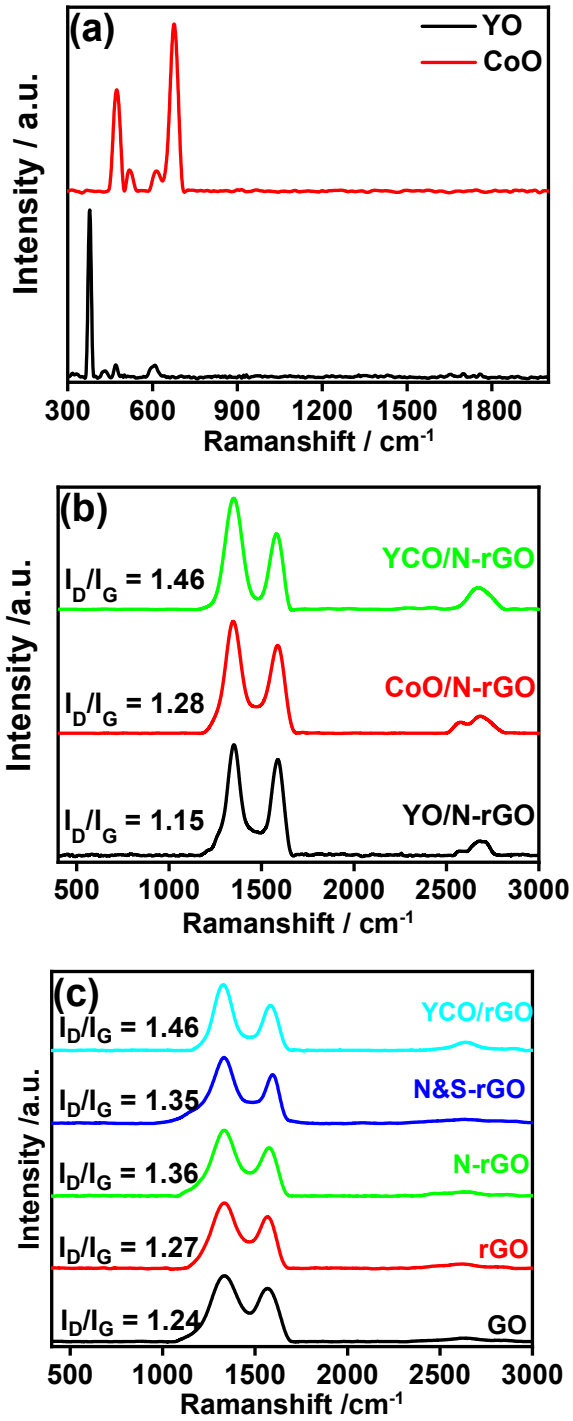

Figure S5. Raman spectra of (a) metal oxides (b) metal oxide/ nitrogen doped composites and (c) other control samples.

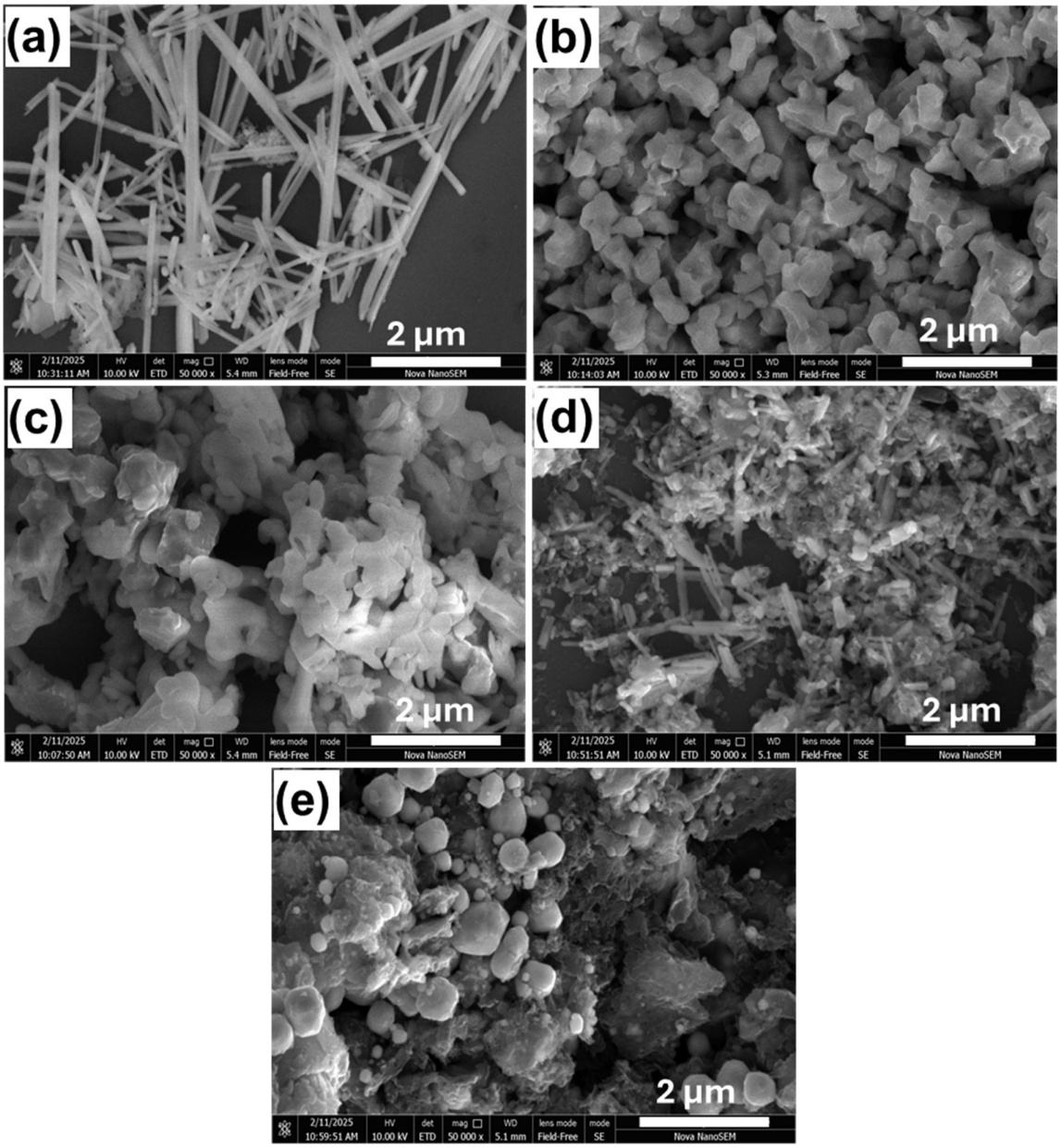

Figure S6. SEM images of (a) Yttrium oxide (YO), (b) cobalt oxide (CoO), (c) Yttrium cobalt oxide (YCO), (d) YO/N&S-rGO and (e) CoO/N&S-rGO.

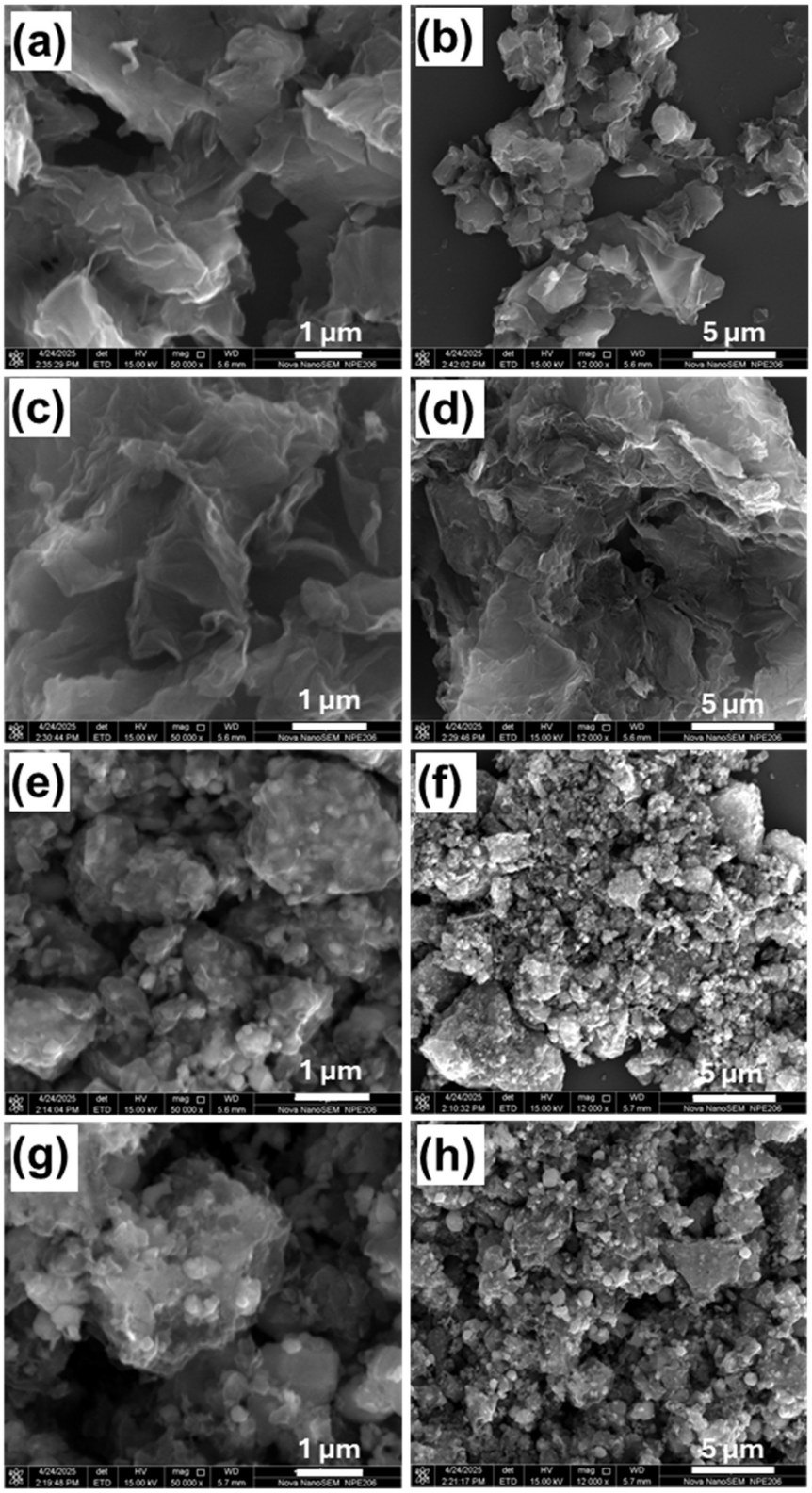

Figure S7. SEM images of (a-b) GO, (c-d) N&S-rGO, (e-f) YCO/N-rGO, and (g-h) YCO/S-rGO

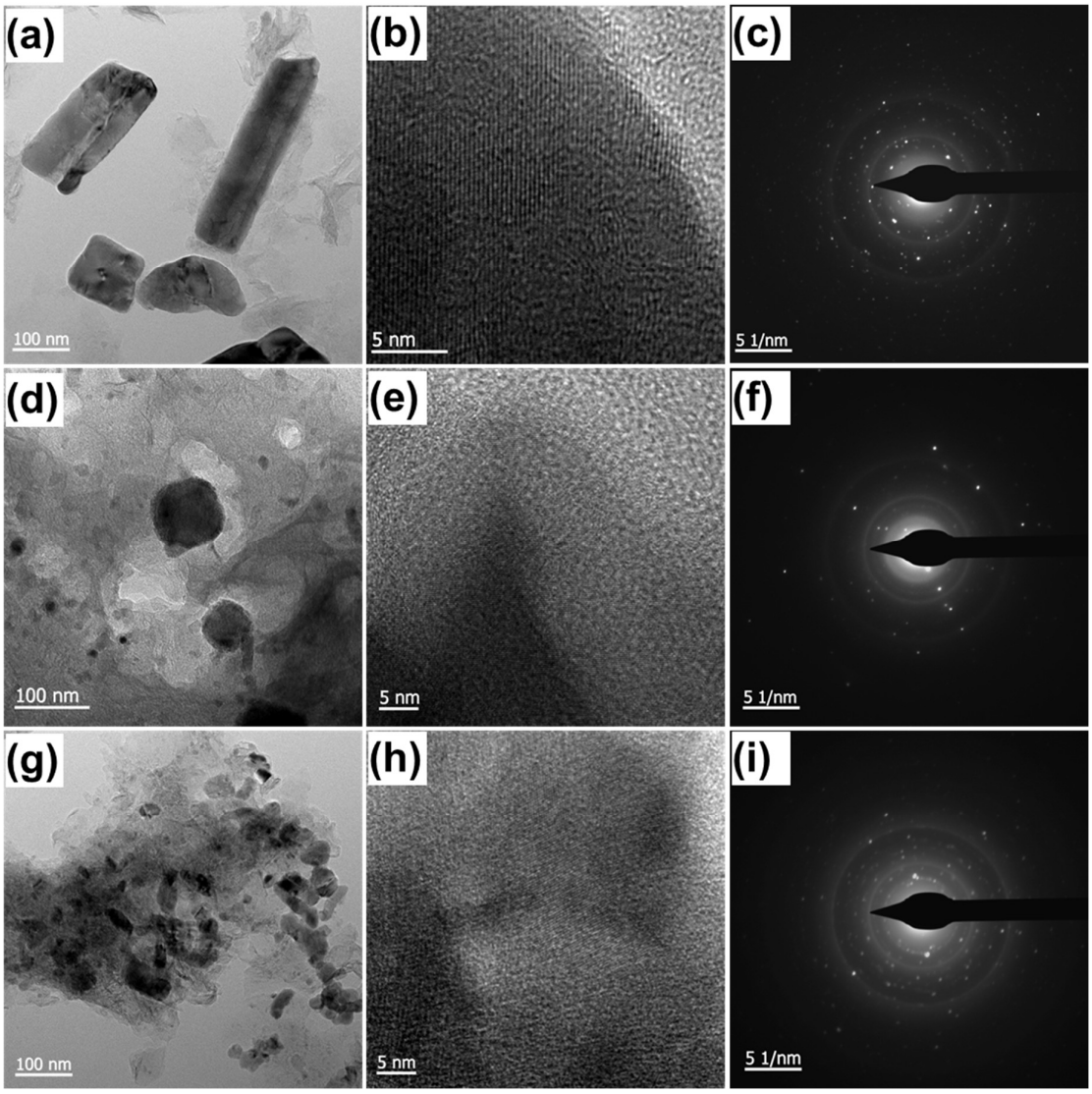

Figure S8. HRTEM and SAED pattern of (a,b,c) YO/N&S-rGO, (d,e,f) CoO/N&S-rGO and (g,h,i) YCO/N&S-rGO respectively.

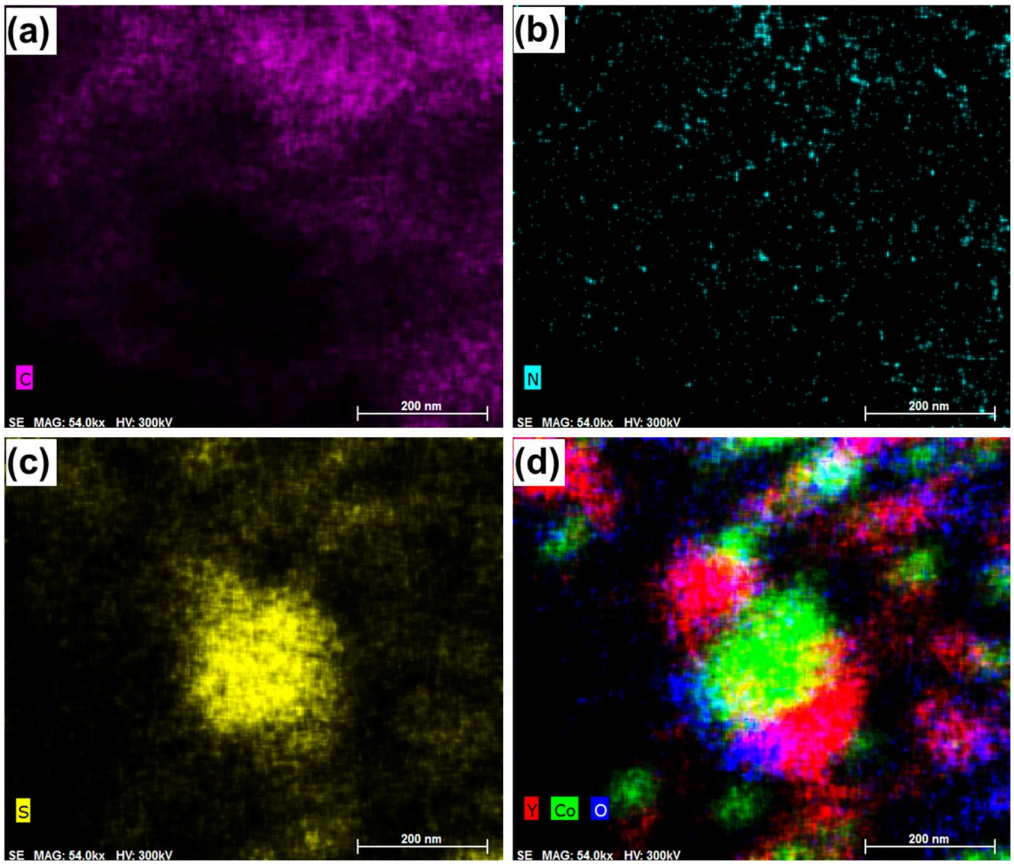

Figure S9. HAADF-STEM EELS elemental mapping of (a) C, (b) N, (c) S and (d) Y, Co & O in YCO/N&S-rGO.

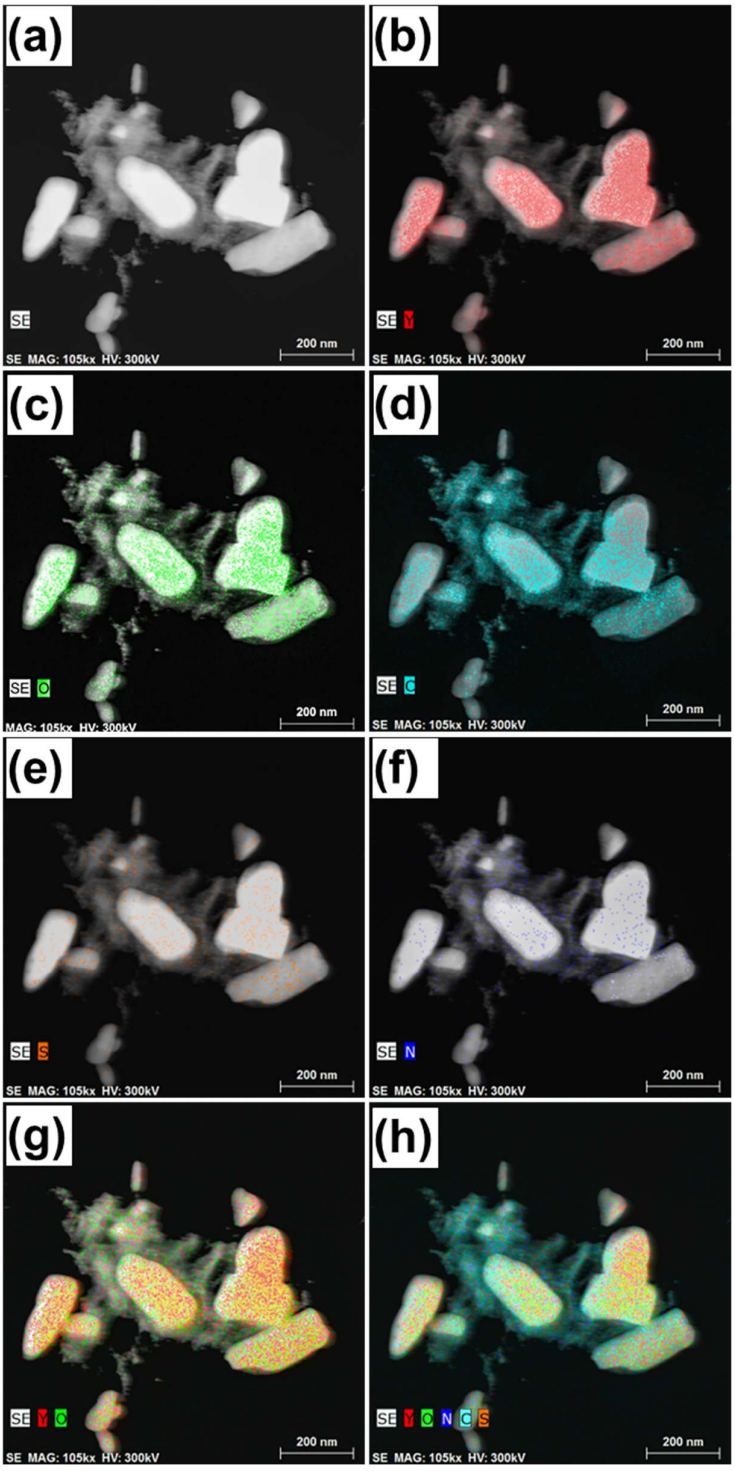

Figure S10. (a) HAADF-STEM image and the corresponding EELS elemental mapping, (b) Y, (c) O, (d) C, (e) S and (f) N. (g) Overlap of (g) Y and O and (h) all elements in YO/N&S-rGO.

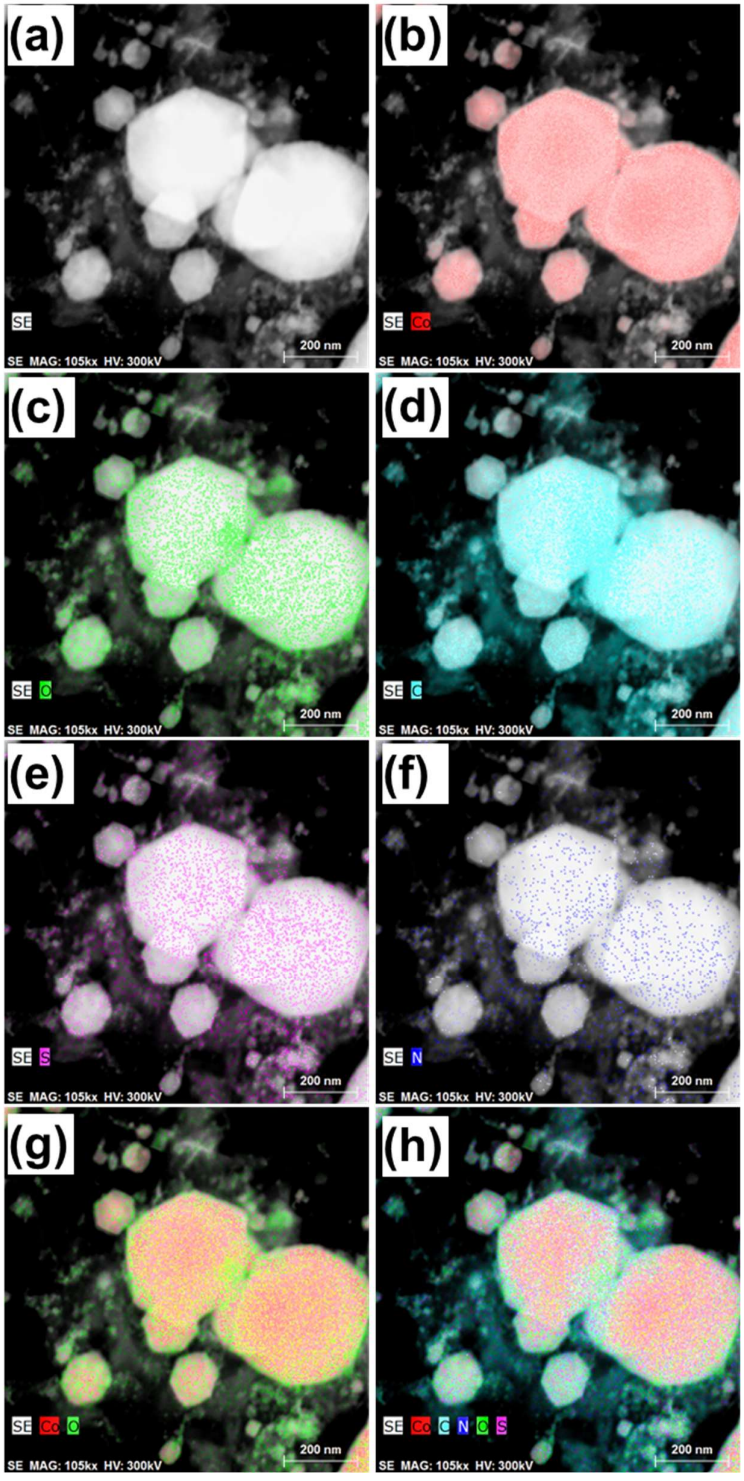

Figure S11. (a) HAADF-STEM image and the corresponding EELS elemental mapping, (b) Co, (c) O, (d) C, (e) S and (f) N. (g) Overlap of Co and O and (h) overall elements in CoO/N&S-rGO.

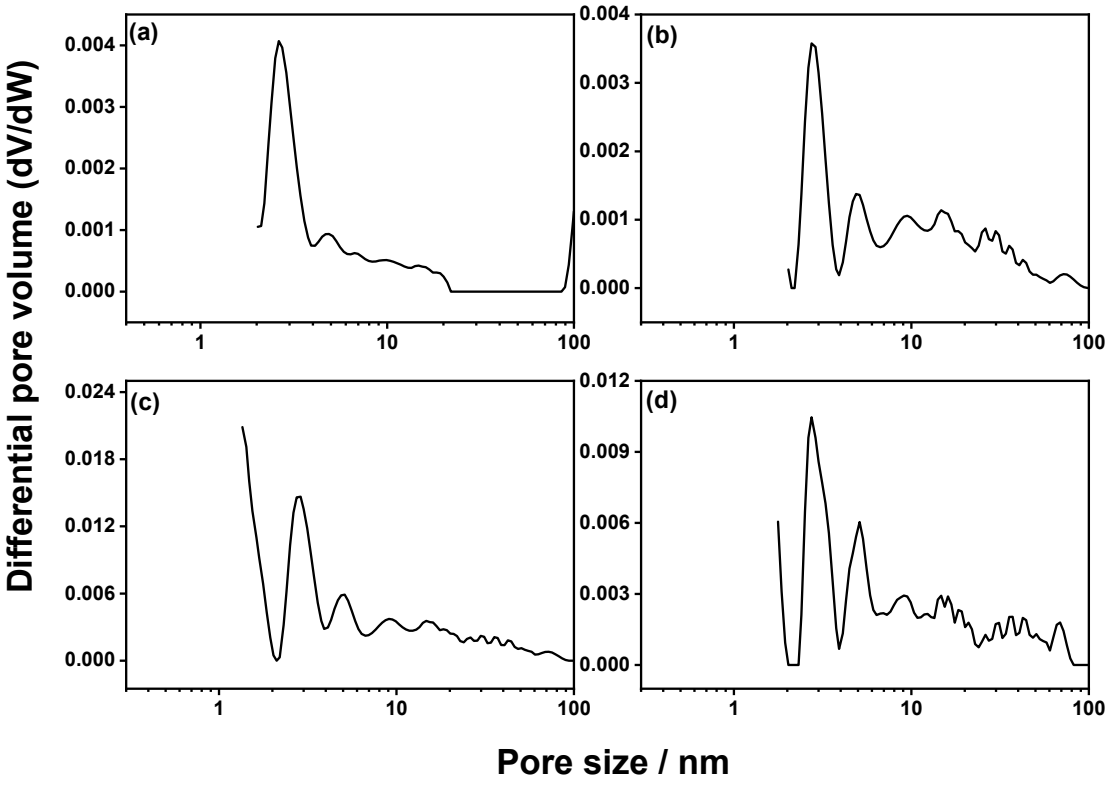

Figure S12. Pore size distribution of synthesized materials (a) YCO, (b) YO/N&S-rGO, (c) CoO/N&S-rGO and (d) YCO/N&S-rGO by NLDFT method.

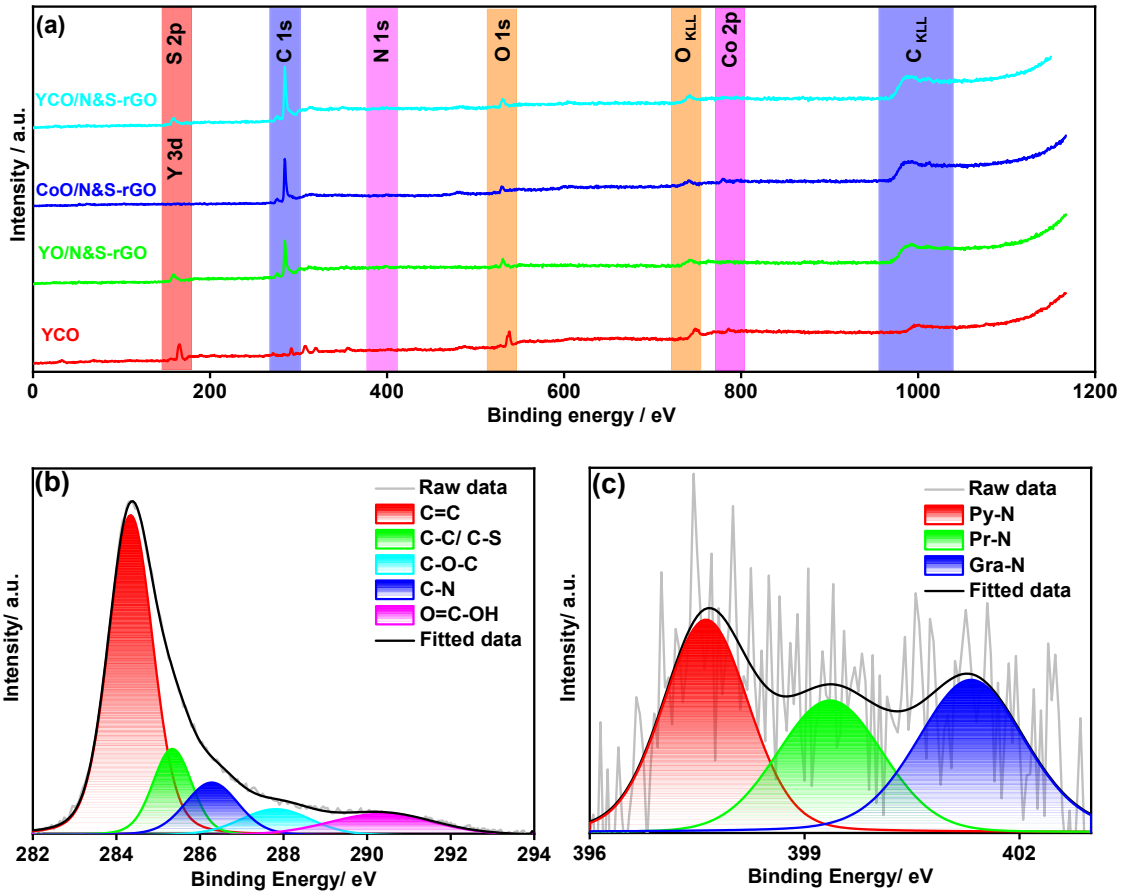

Figure S13. (a) XPS survey spectra of YCO, YO/N&S-rGO, CoO/N&S-rGO and YCO/N&S-rGO, Core level deconvoluted spectra of (b) C-1s and (c) N-1s XPS of YCO/N&S-rGO.

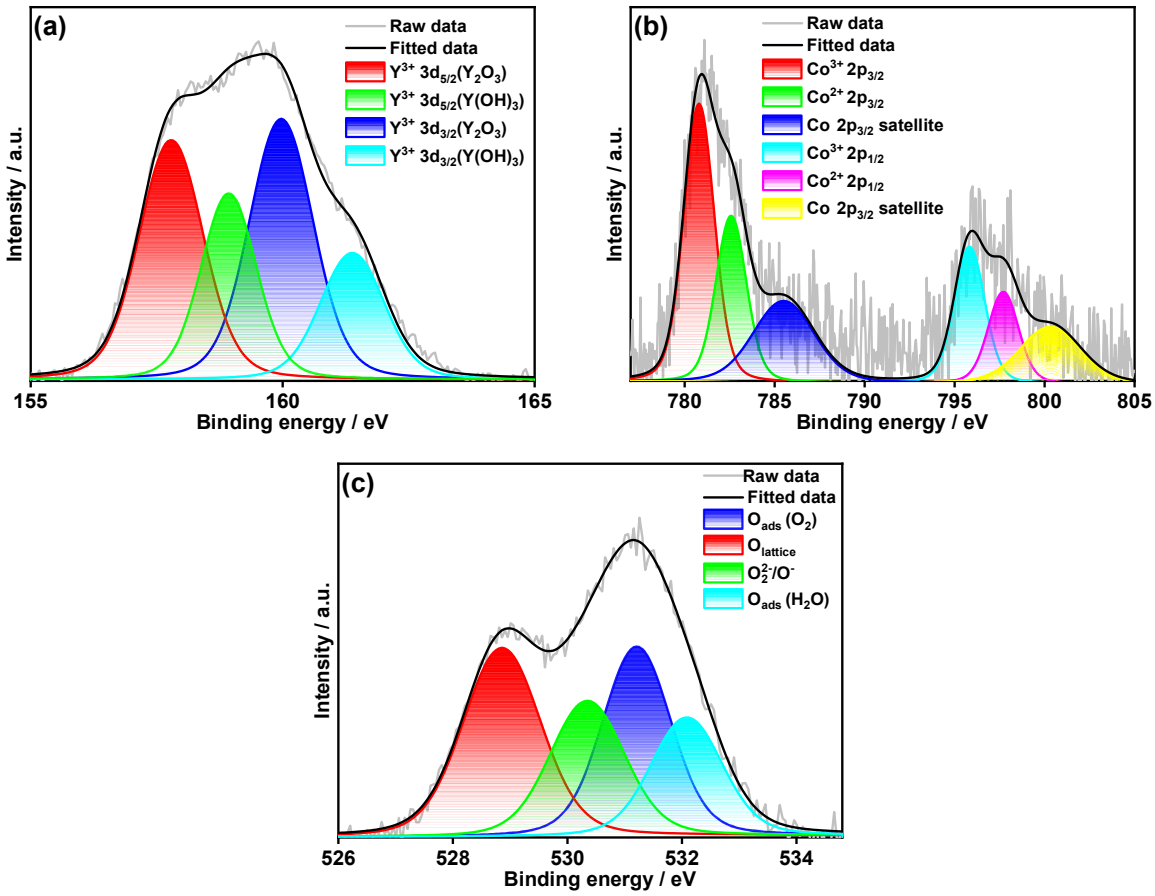

Figure S14. Core level deconvoluted spectra of (a) Y-3d, (b) Co-2p and (c) O-1s of YCO.

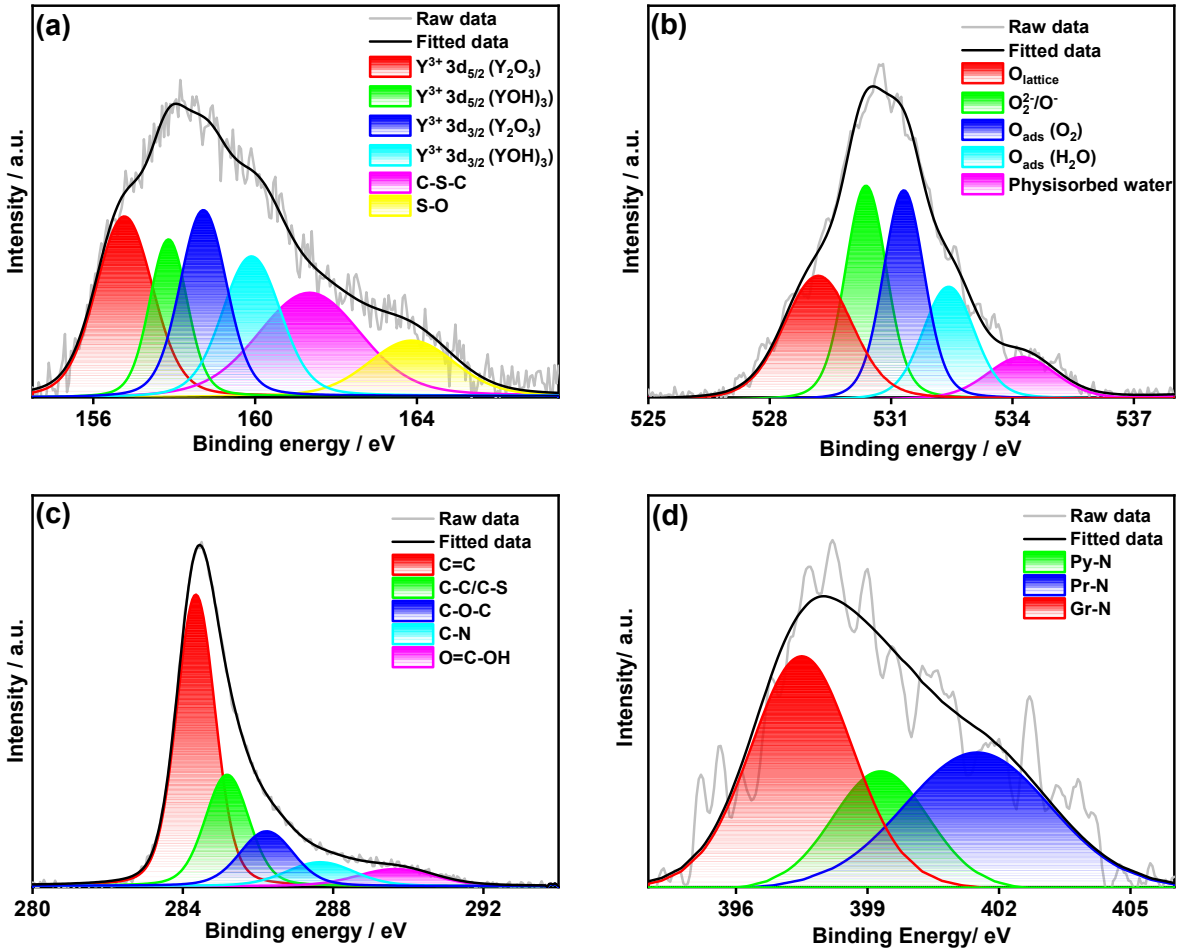

Figure S15. Core level deconvoluted spectra of (a) Y-3d & S-2p, (b) O-1s, (c) C-1s and (d) N-1s of YO/N&S-rGO.

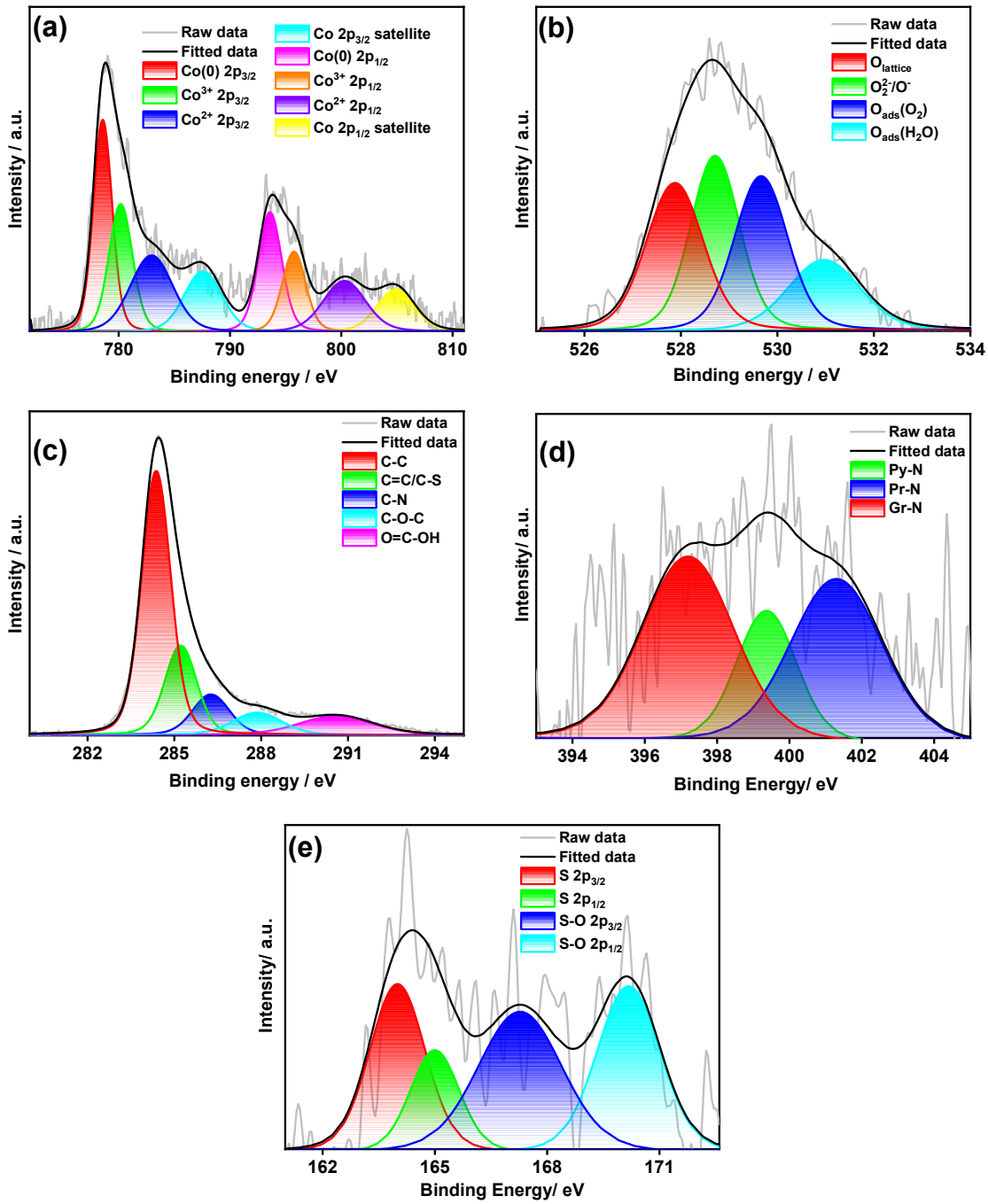

Figure S16. Core level deconvoluted spectra of (a) Co-2p, (b) O-1s, (c) C-1s, (d) N 1s and € S 2p of CoO/N&S-rGO.

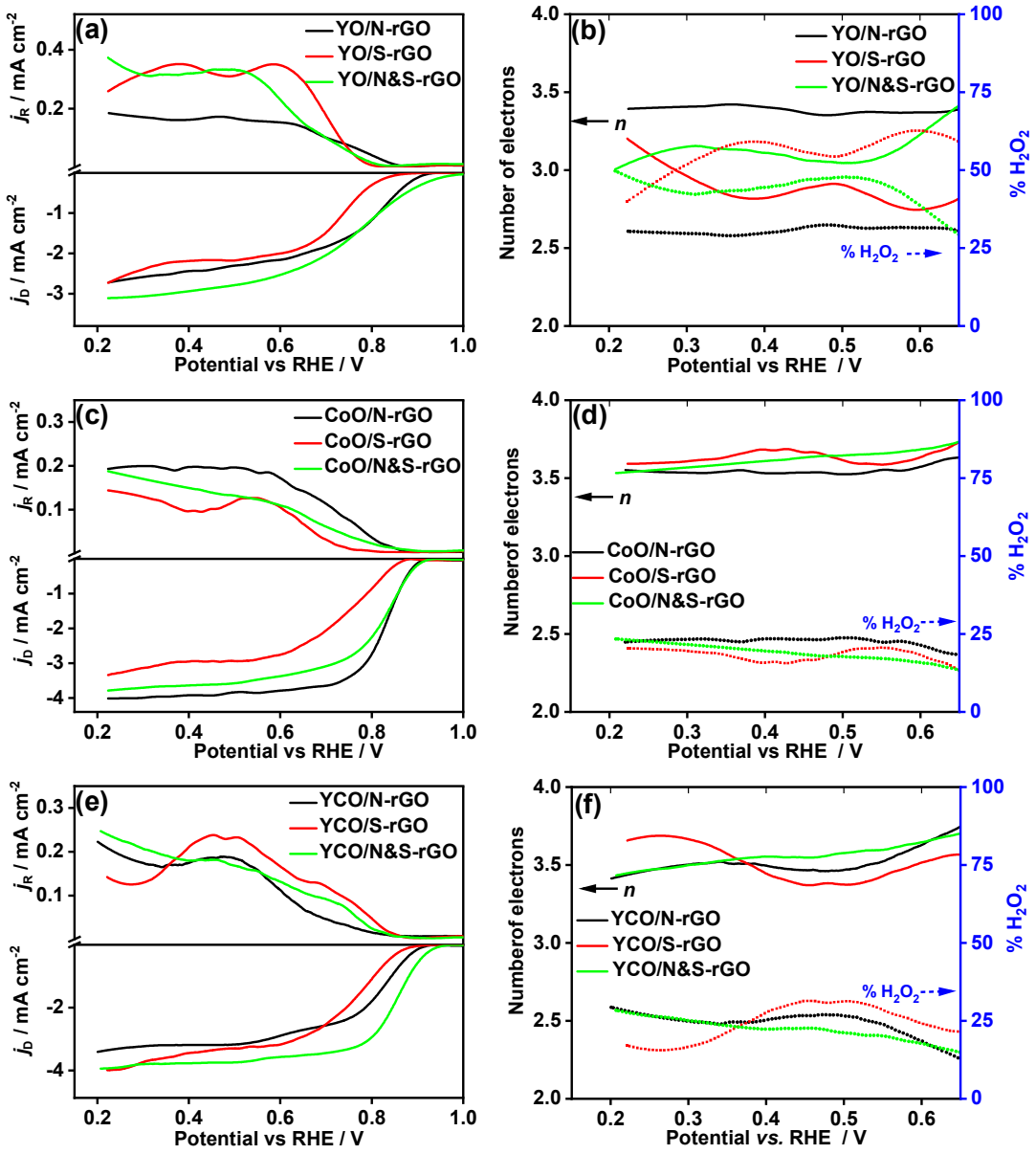

Figure S17. The RRDE voltammograms of ORR in O_2-saturated 0.1 M KOH on (a) yttria carbon composites, (c) cobalt oxide carbon composites and (e) YCO carbon composites. (b), (d) and (f) are the potential dependent number of electrons and % H_2O_2 of the yttria, cobalt oxide and YCO carbon composites, respectively. The electrode rotational speed is 1600 rpm, and the scan rate is 10 mV s^{-1}. The Pt-ring electrode was kept at a constant potential of 1.2 V.

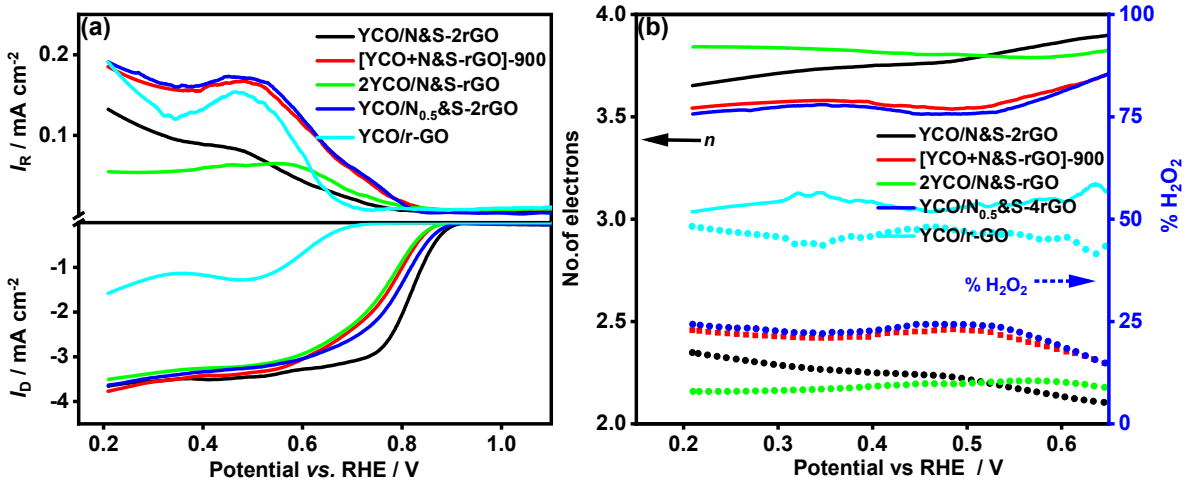

Figure S18. (a) The RRDE voltammograms of ORR (O_2 saturated 0.1 M KOH) on control samples (varying the precursor content) at 1600 rpm (scan rate 10 mV s^{-1}) and (b) corresponding number of electrons and % H_2O_2.

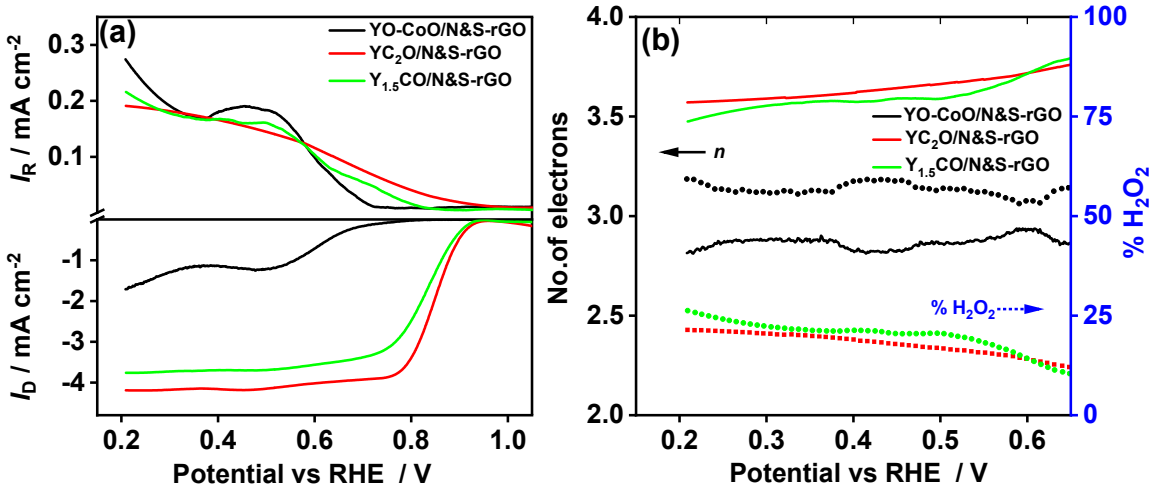

Figure S19. (a) The RRDE voltammograms of ORR (O_2 saturated 0.1 M KOH) on control samples (varying the metal content) at 1600 rpm (scan rate 10 mV s^{-1}) and (b) corresponding number of electrons and % H_2O_2.

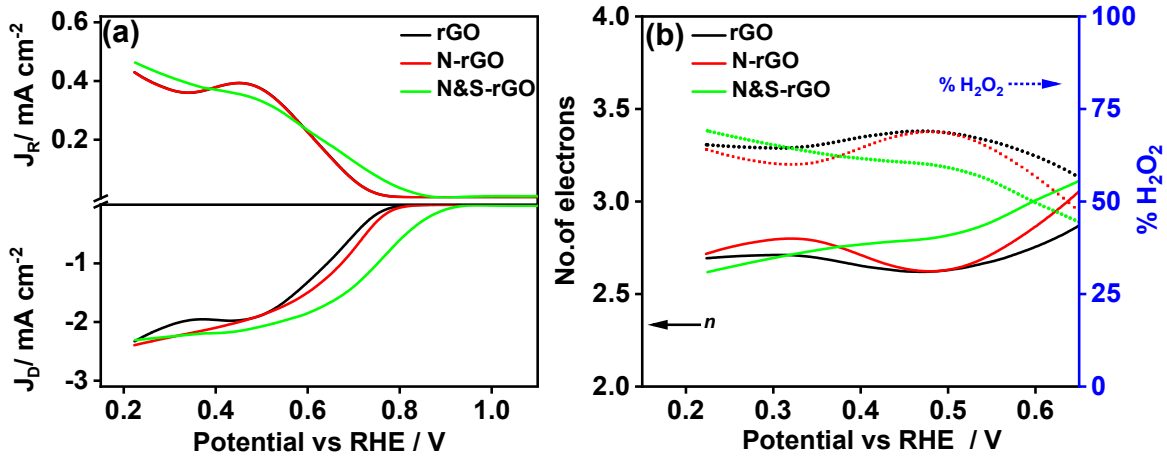

Figure S20. (a) The RRDE voltammograms of ORR (O_2 saturated 0.1 M KOH) on control samples (undoped and heteroatom atom(s) doped carbon materials) at 1600 rpm (scan rate 10 mV s^{-1}) and (b) corresponding number of electrons and % H_2O_2.

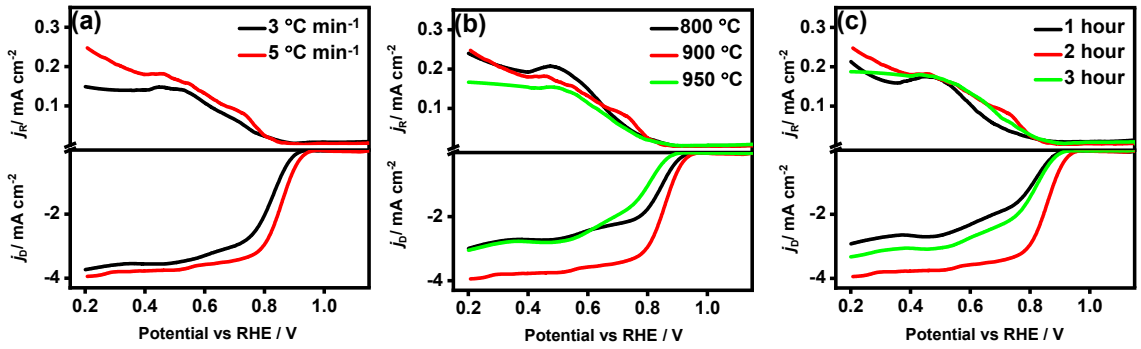

Figure S21. The RRDE voltammograms of YCO/N&S-rGO at 1600 rpm rotational speed (scan rate 10 mV s^{-1}) in O_2-saturated 0.1 M KOH electrolyte by varying the parameter (a) at different ramp rates, (b) at different temperatures, and (c) at different dwelling times, of heat treatment in the N_2 atmosphere.

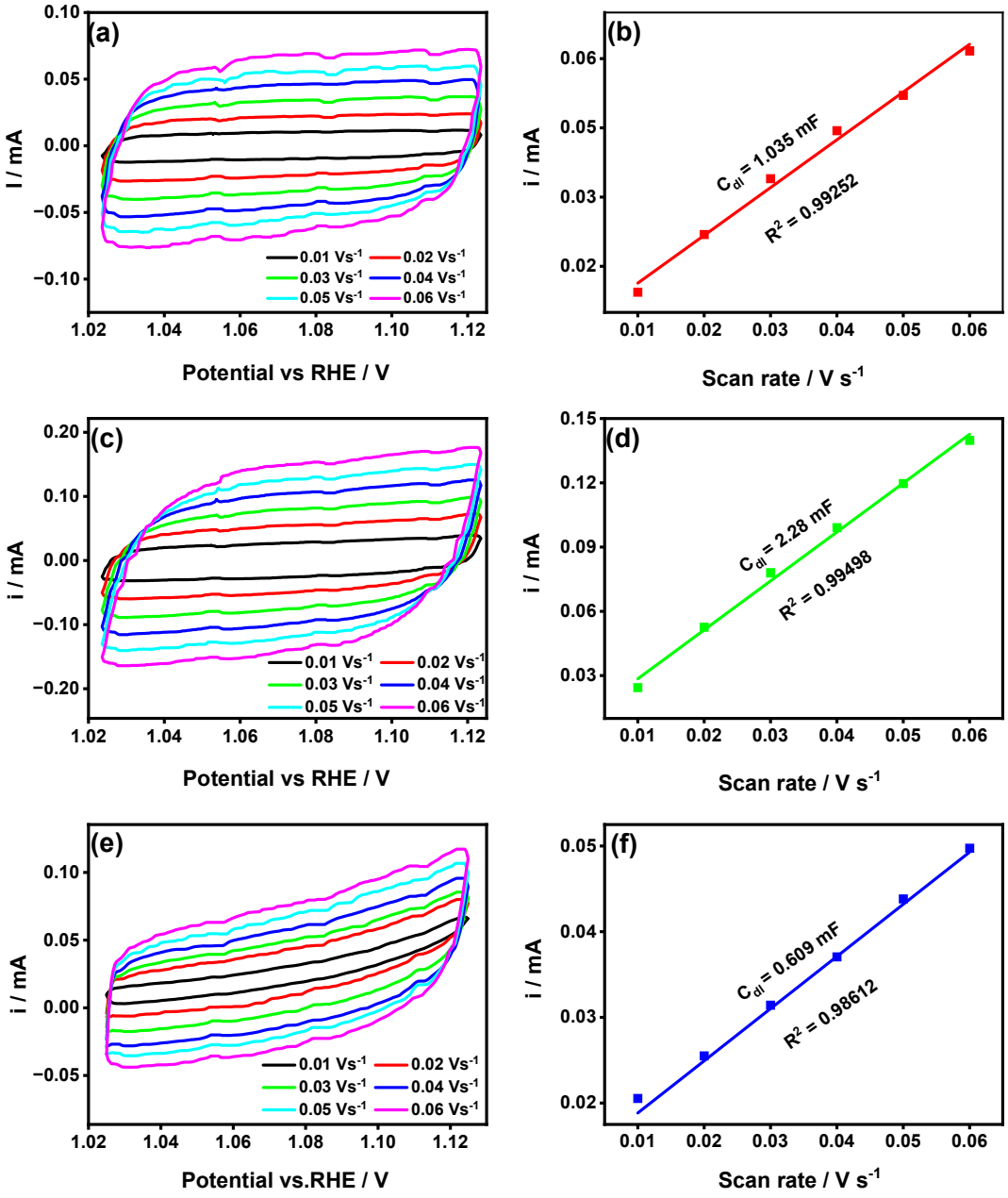

Figure S22. Cyclic voltammograms measured in the non-Faradaic region at different scan rates and the scan rate vs current (average of cathodic and anodic charging currents is measured at 1.055 V vs RHE) plots for double-layer capacitance measurements of (a) & (b) YO/N&S-rGO, (c) & (d) CoO/N&S-rGO and (e) & (f) YCO/N&S-rGO in 1 M KOH. The determined double-layer capacitance of the system is taken as the slope of the linear fits to the data.

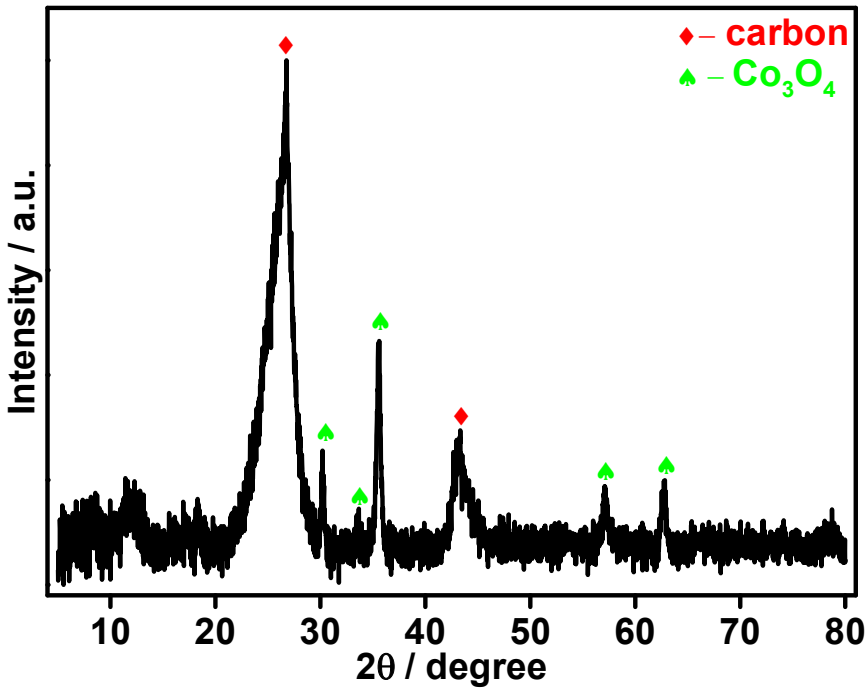

Figure S23. The powder XRD patterns of acid-washed YCO/N&S-rGO (diffraction peaks were separately labelled)

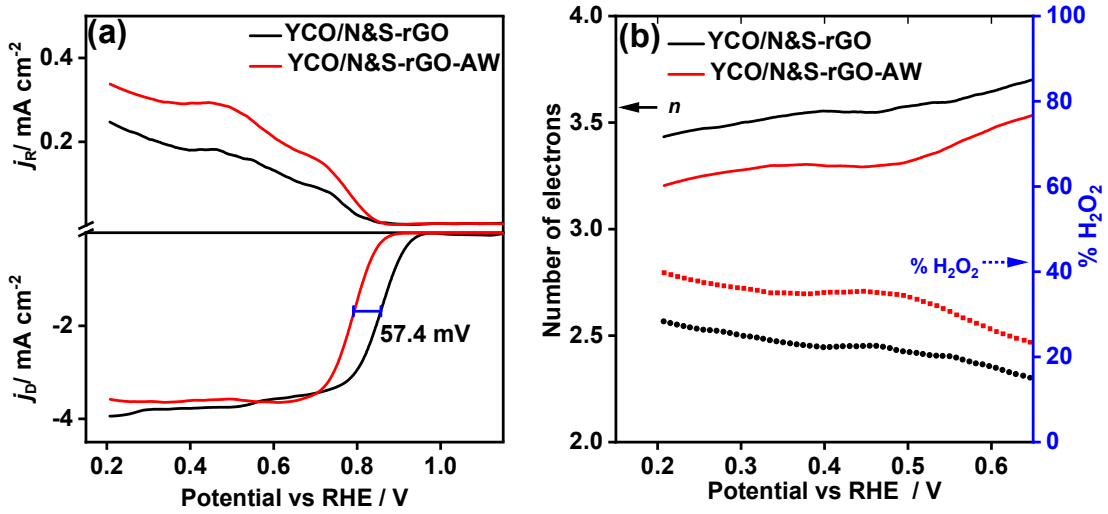

Figure S24. (a) The RRDE voltammograms of acid-washed YCO/N&S-rGO in comparison with YCO/N&S-rGO in O_2 saturated 0.1 M KOH at 1600 rpm (scan rate 10 mV s^{-1}) and (b) corresponding number of electrons and % H_2O_2.

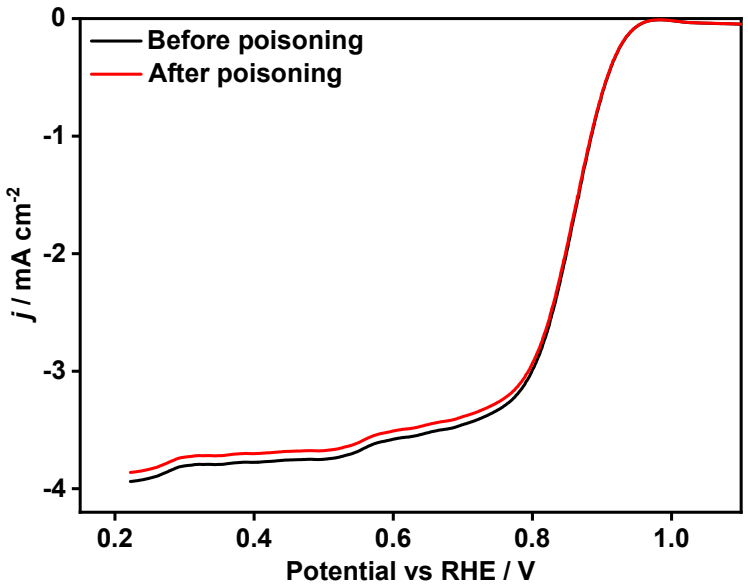

Figure S25. RDE voltammograms of YCO/N&S-rGO at 1600 rpm rotational speed (scan rate 10 mV s^{-1}) in O_2-saturated in 0.1 M KOH and 10 mM KSCN+0.1 M KOH electrolyte.

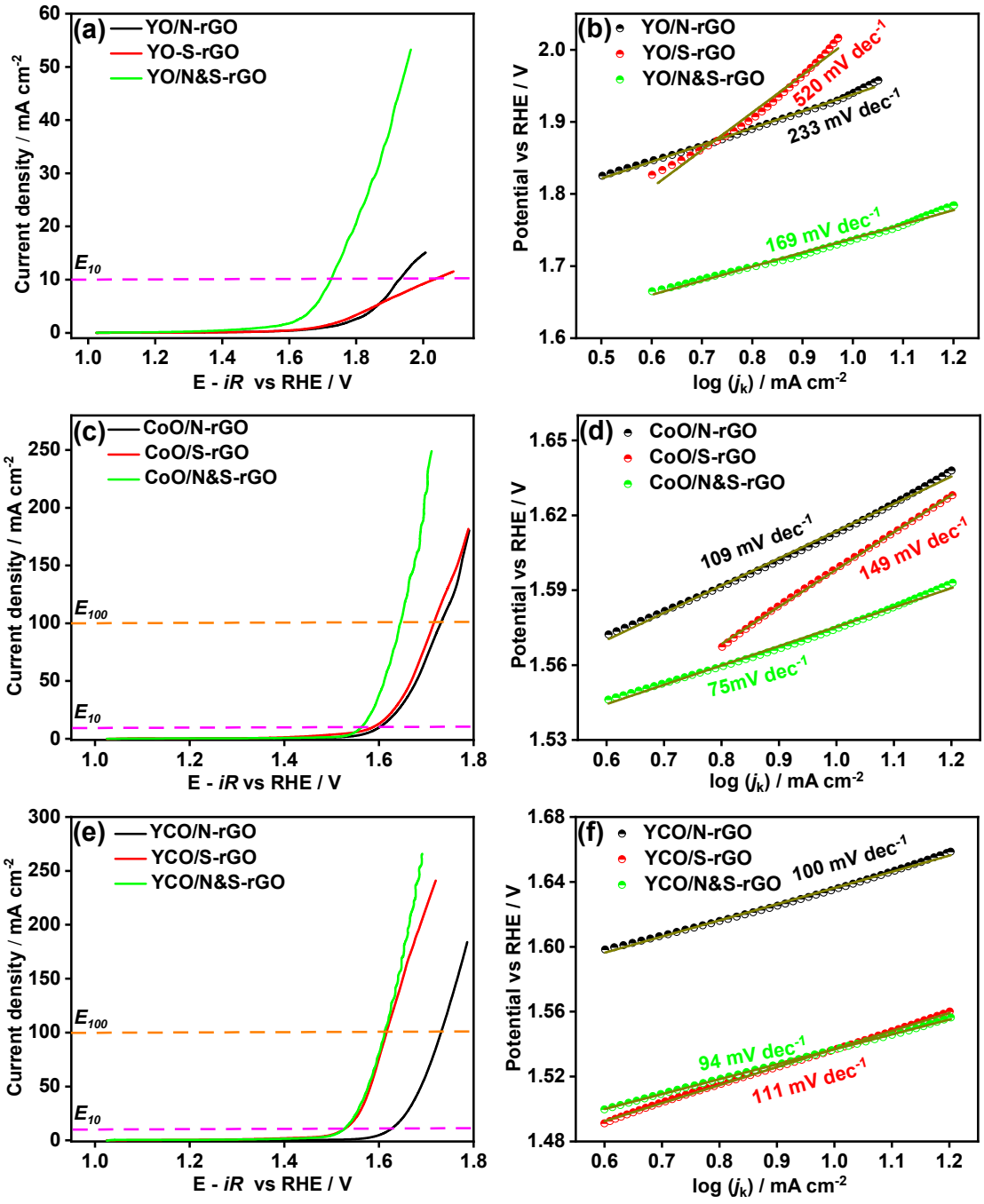

Figure S26. The linear sweep voltammograms (with 80 % *iR* compensation) of OER on (a,c,e) heteroatom-doped metal oxides in 1 M KOH at 2000 rpm (scan rate 10 mV s^{-1}) and (b,d,f) the corresponding Tafel plots.

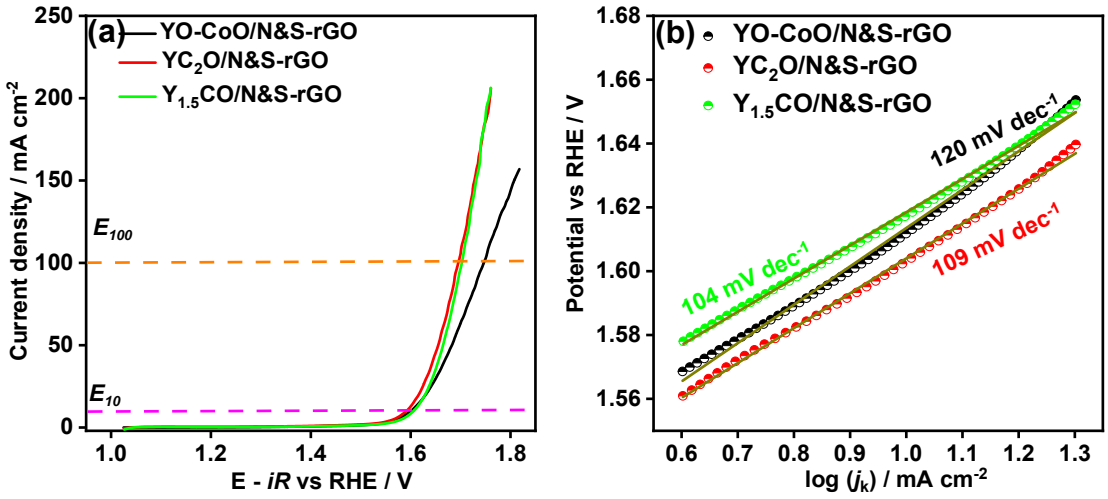

Figure S27. (a) The linear sweep voltammograms of OER (with 80 % *iR* compensation) on control samples (varying the metal content) in 1 M KOH at 2000 rpm (scan rate 10 mV s^{-1}) and (b) corresponding Tafel plot.

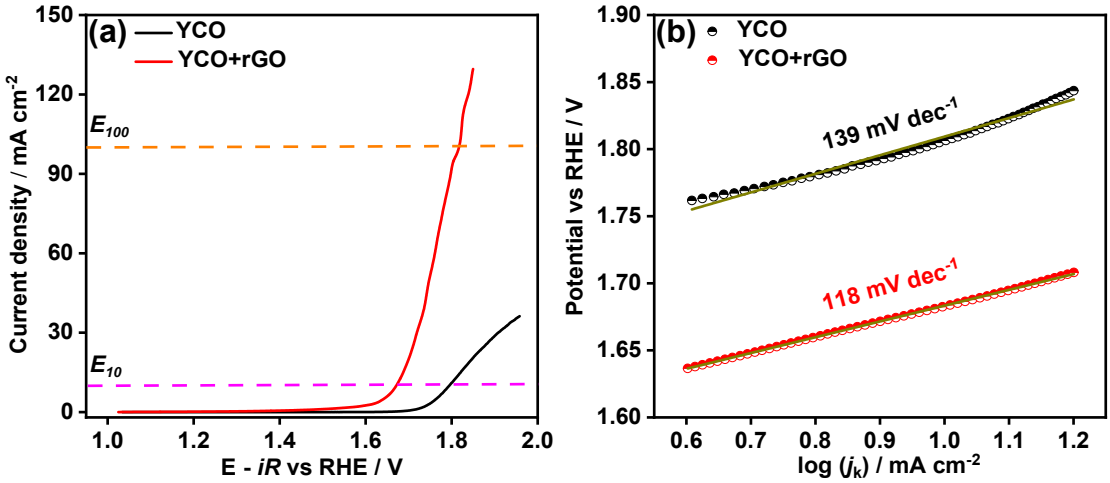

Figure S28. The linear sweep voltammograms of OER (with 80 % *iR* compensation) on YCO and YCO+rGO in 1 M KOH electrolyte at 2000 rpm (scan rate 10 mV s^{-1}) and their (b) Tafel plots.

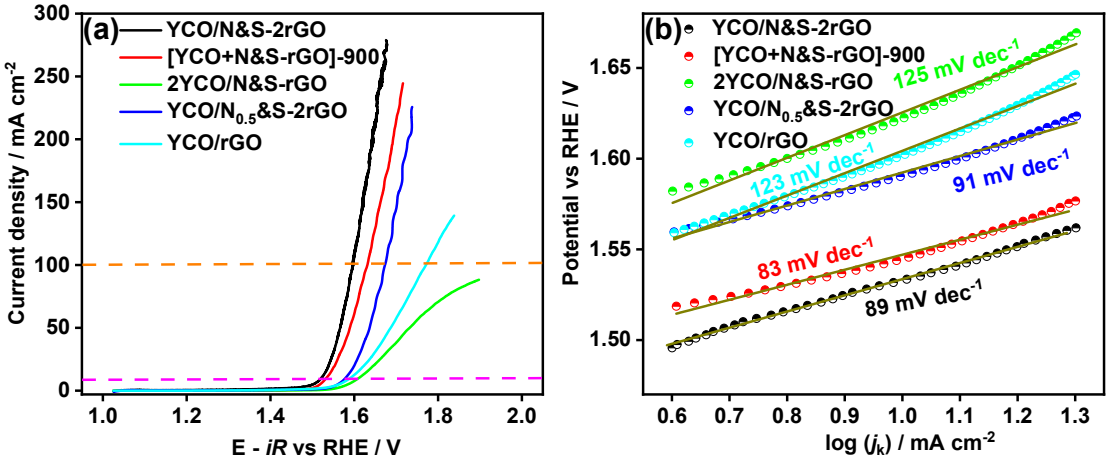

Figure S29. (a) The linear sweep voltammograms of OER (with 80 % *iR* compensation) on control samples (varying the precursor content) in 1 M KOH at 2000 rpm (scan rate 10 mV s^{-1}) and (b) corresponding Tafel plot.

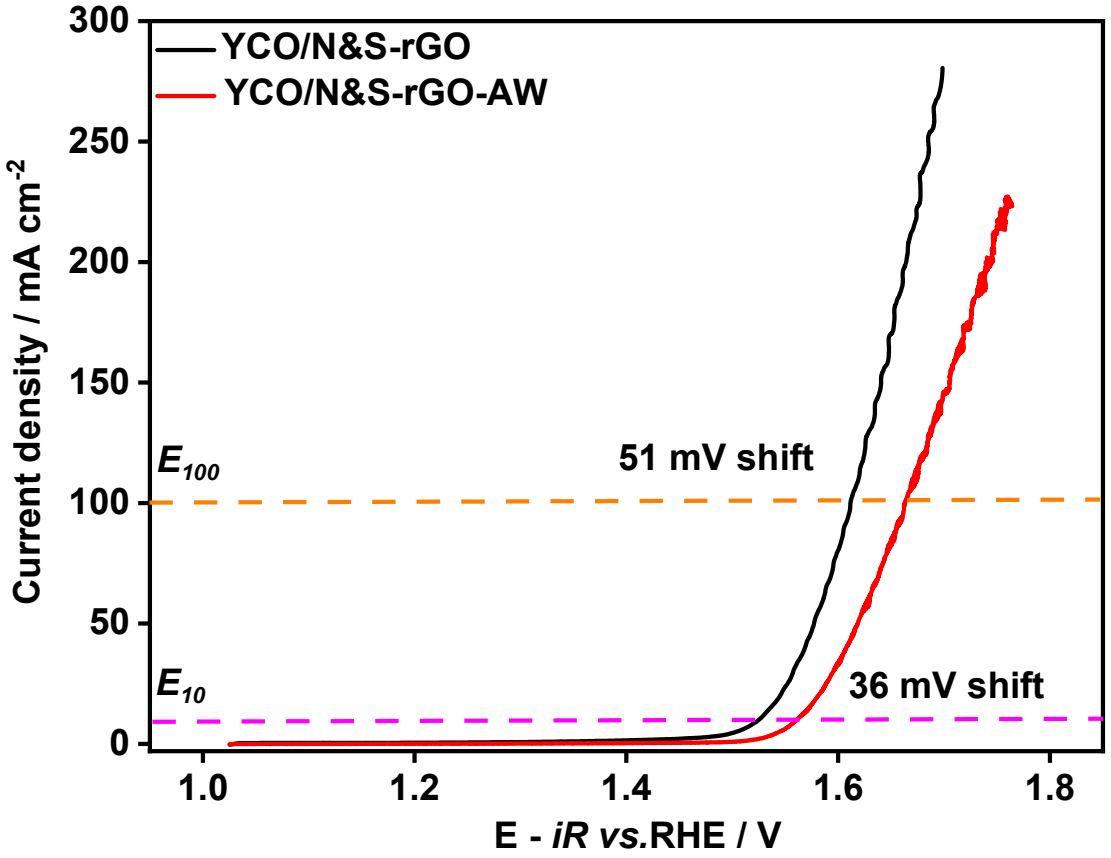

Figure S30. (a) The linear sweep voltammograms (with 80 % *iR* compensation) of OER of acid-washed YCO/N&S-rGO in comparison with YCO/N&S-rGO in 1 M KOH at 2000 rpm (scan rate 10 mV s^{-1}).

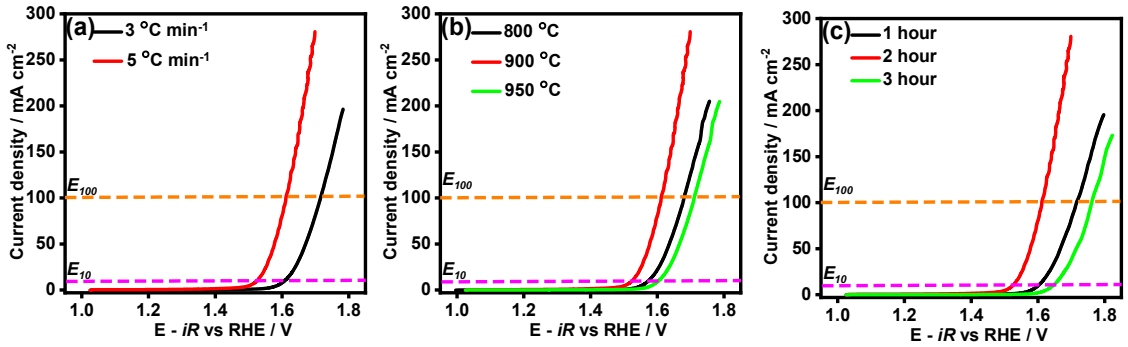

Figure S31. The linear sweep voltammograms of OER (with 80 % *iR* compensation) on by varying the parameter (a) at different ramp rates, (b) at different temperatures, and (c) at different dwelling times, of heat treatment in the N_2 atmosphere in 1 M KOH at 2000 rpm (scan rate 10 mV s^{-1}).

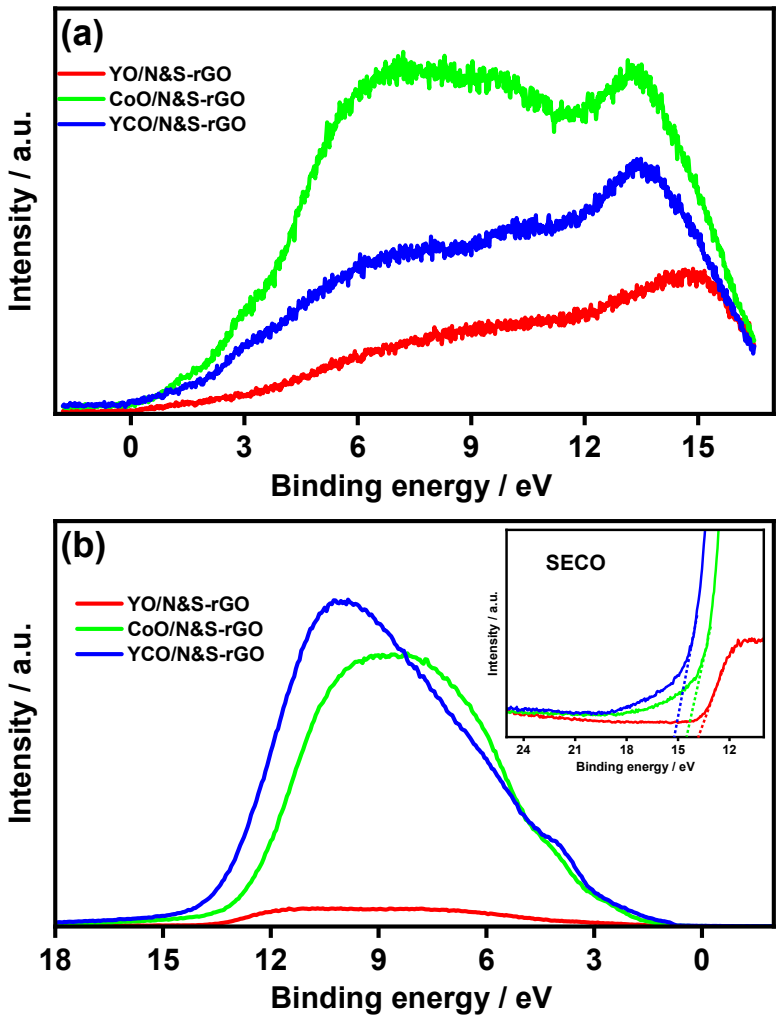

Figure S32. The complete UPS spectra (a) without the application of bias voltage and (b) with the application of bias voltage of -17.9 V with enlarged spectral parts near the Fermi edge and near the cut-off edge as an inset.

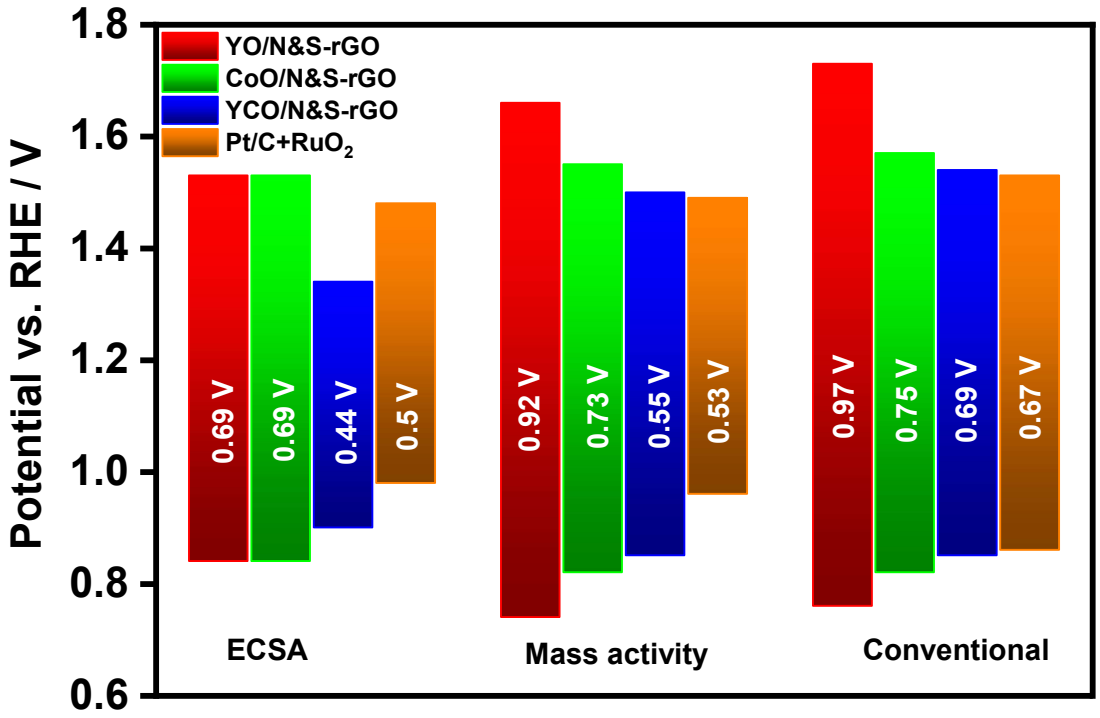

Figure S33. The ΔE values calculated for the synthesised materials in comparison with the benchmark (Pt/C+RuO_2) catalyst. The ECSA- specific (estimated at 10 μA cm^{-2} of OER and ORR), conventional ($\Delta E = E_{10}^{OER} - E_{1/2}^{ORR}$) and mass-specific kinetic current densities (estimated at 10 A g^{-1} for OER and ORR).

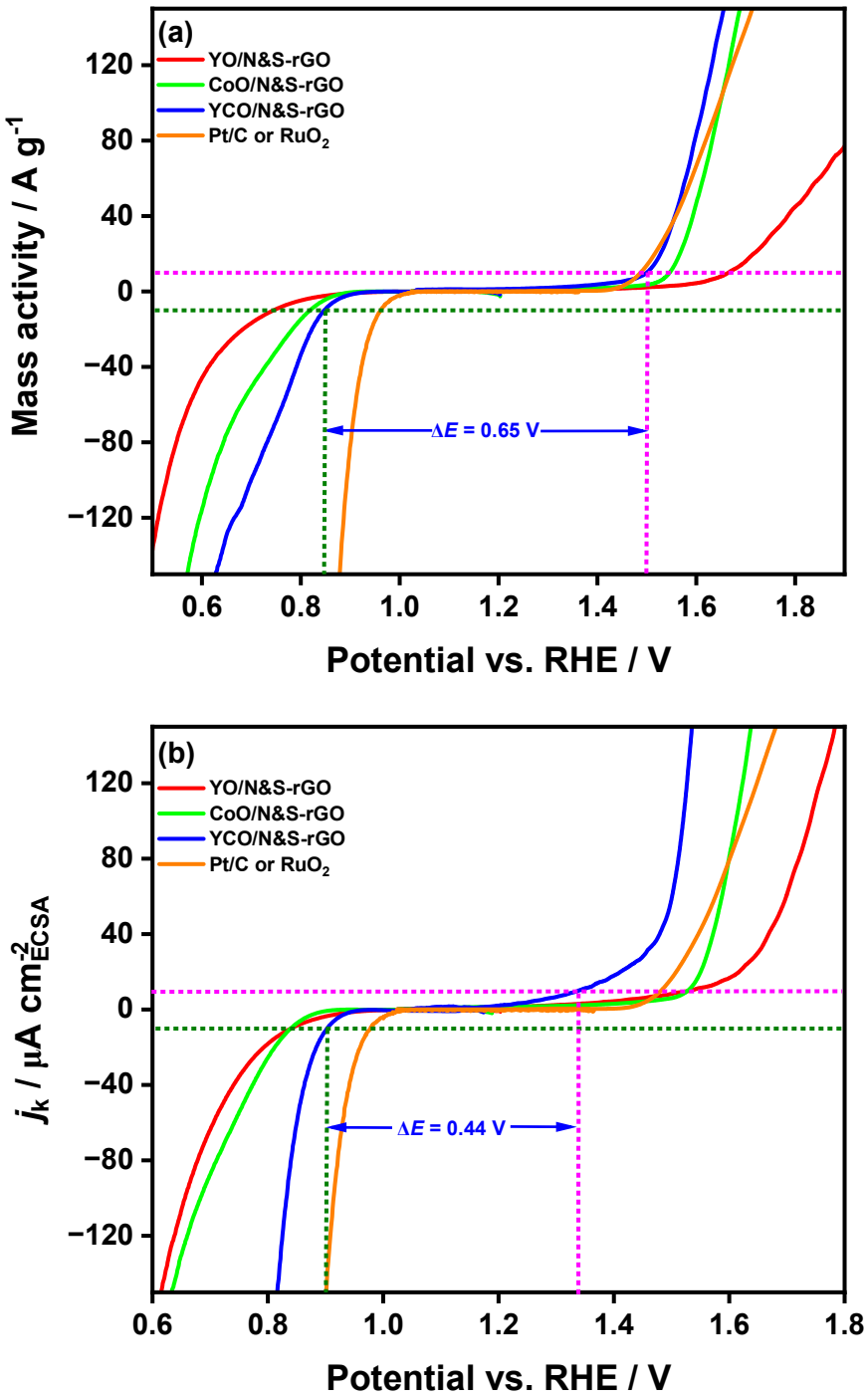

Figure S34. RDE voltammograms of the synthesized materials in the ORR and OER regions, along with the estimated potential gap (ΔE), calculated as the difference between the potentials required to reach (a) 10 A g^{-1} (mass-specific current density) and (b) 10 μA cm^{-2} (ECSA-specific current density) for the OER and ORR.

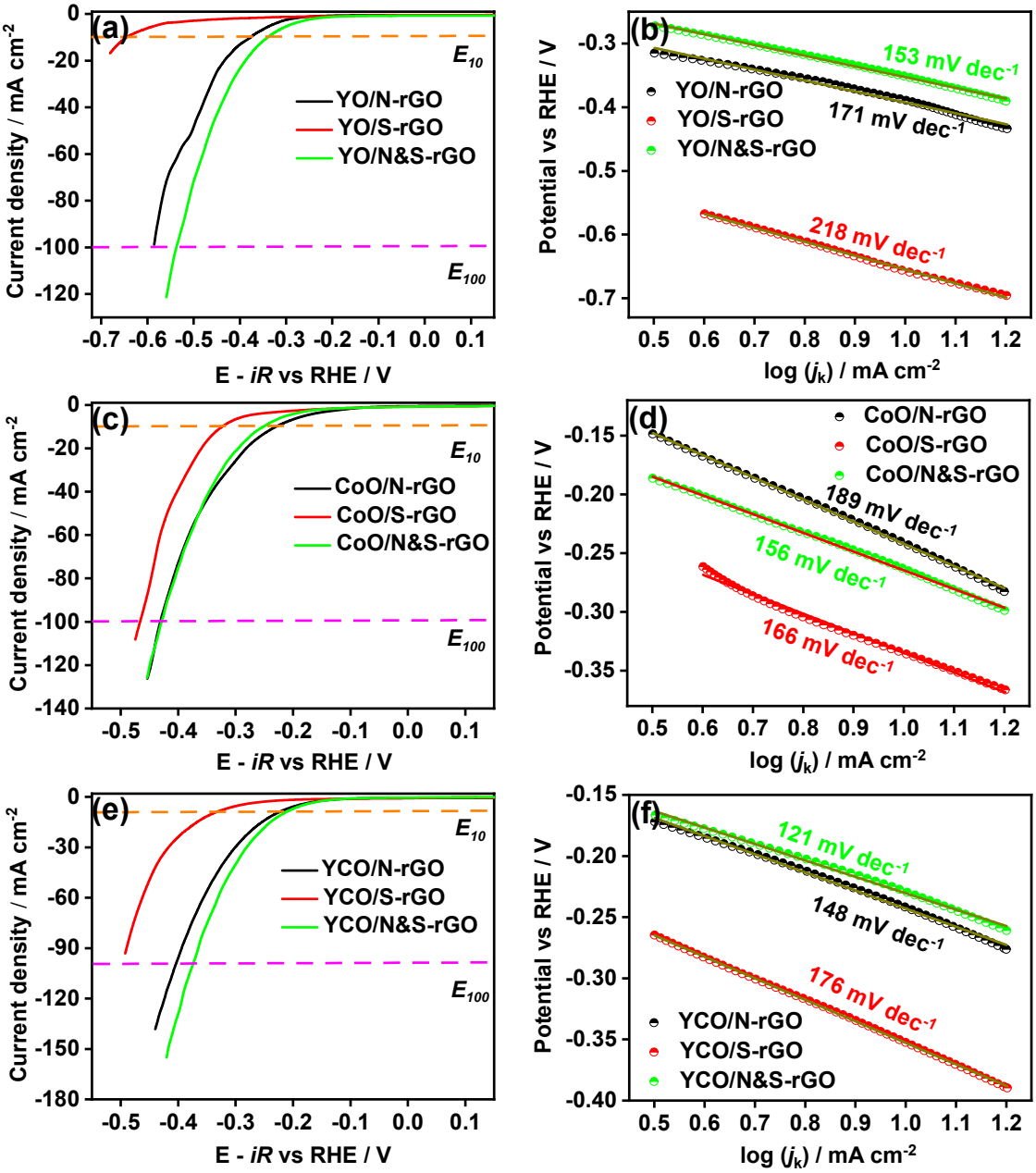

Figure S35. The linear sweep voltammograms of HER (with 80 % *iR* compensation) on (a,c,e) heteroatom doped metal oxides in 1 M KOH at 2000 rpm (scan rate 10 mV s^{-1}) and (b,d,f) the corresponding Tafel plots.

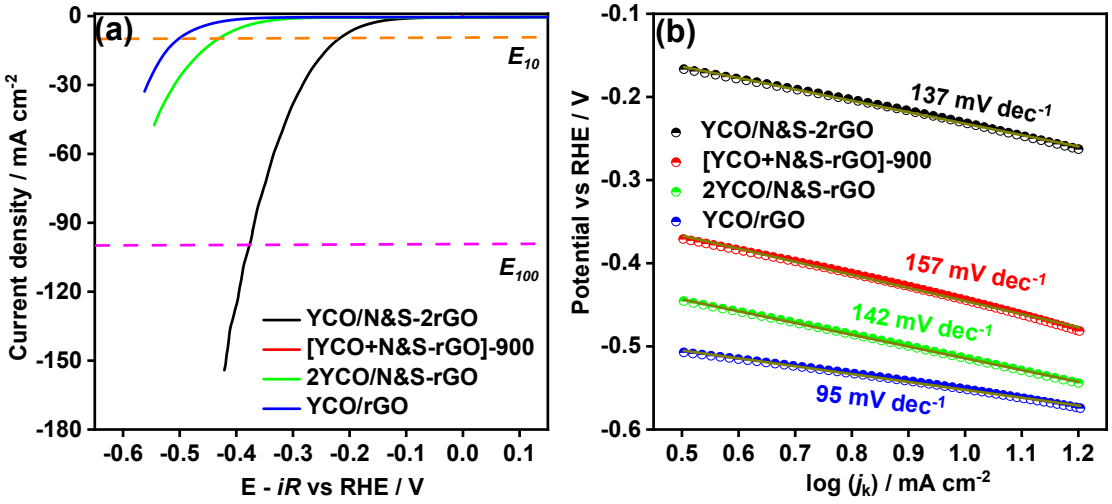

Figure S36. (a) The linear sweep voltammograms of HER (with 80 % *iR* compensation) on the control samples (varying the precursor content) in 1 M KOH at 2000 rpm (scan rate 10 mV s^{-1}) and (b) corresponding Tafel plot.

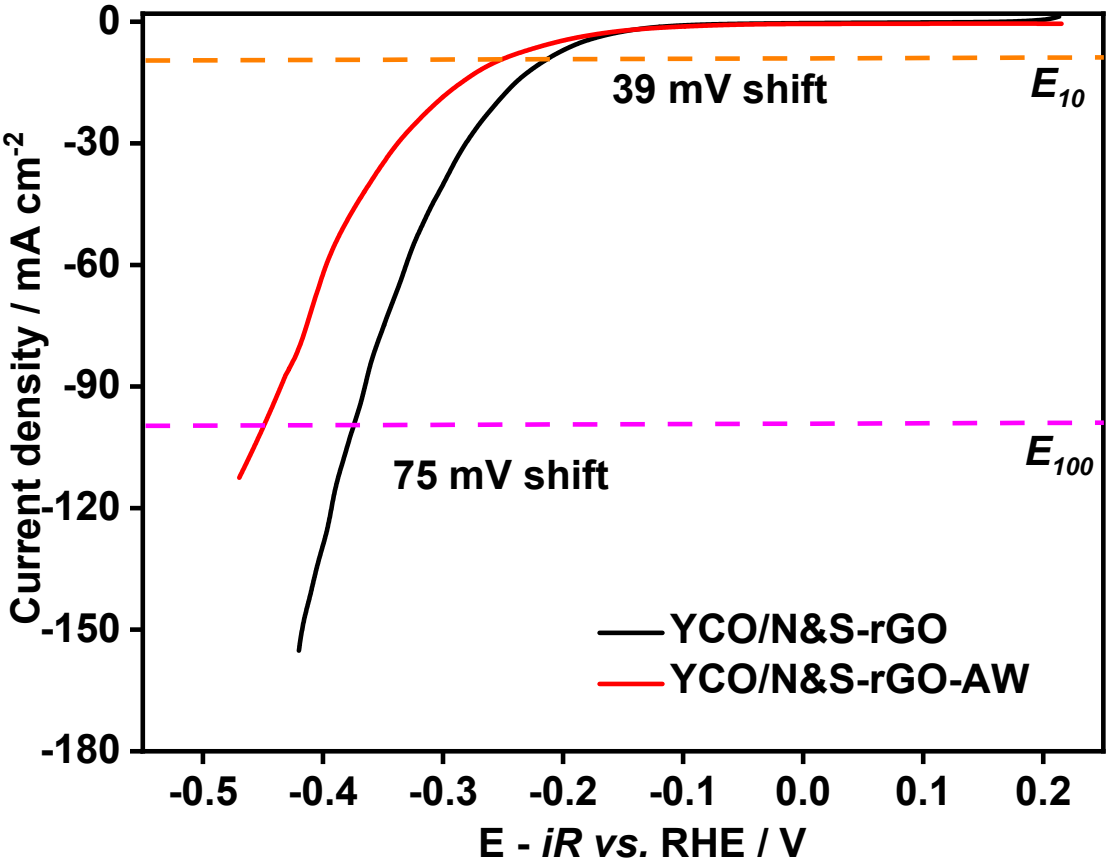

Figure S37. (a) The linear sweep voltammograms of HER (with 80 % *iR* compensation) of acid-washed YCO/N&S-rGO in comparison with YCO/N&S-rGO in 1 M KOH at 2000 rpm (scan rate 10 mV s^{-1}).

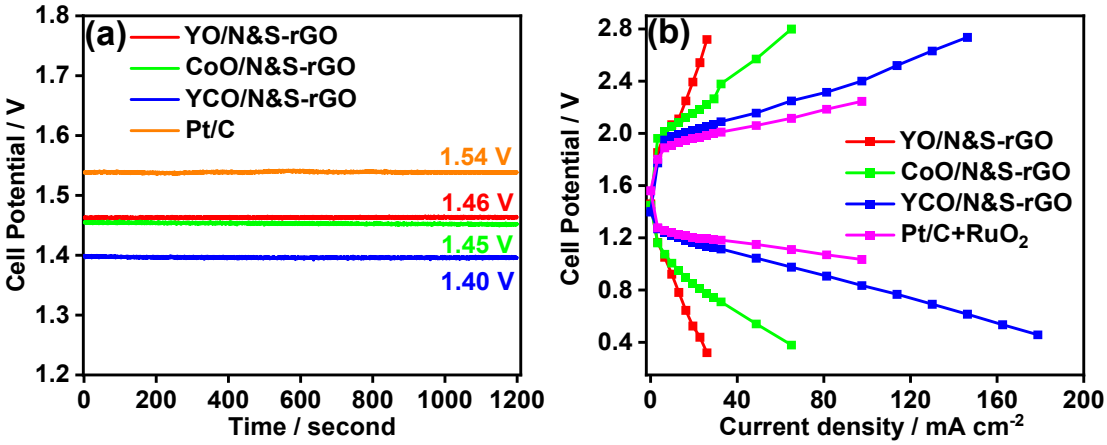

Figure S38. The performance of the liquid electrolyte zinc-air battery using (a) open circuit potential, and (b) charging and discharging profiles of synthesised materials.

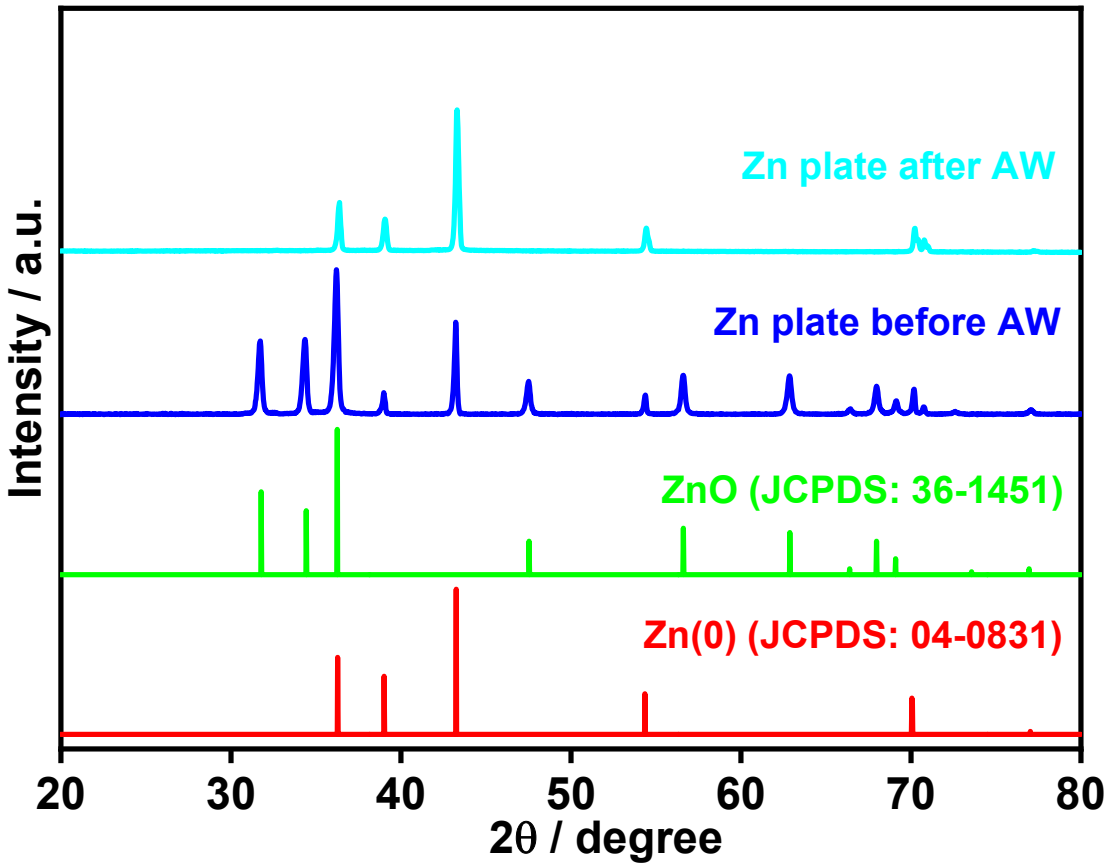

Figure S39. The PXRD pattern of Zn plate measured after the specific capacity measurement

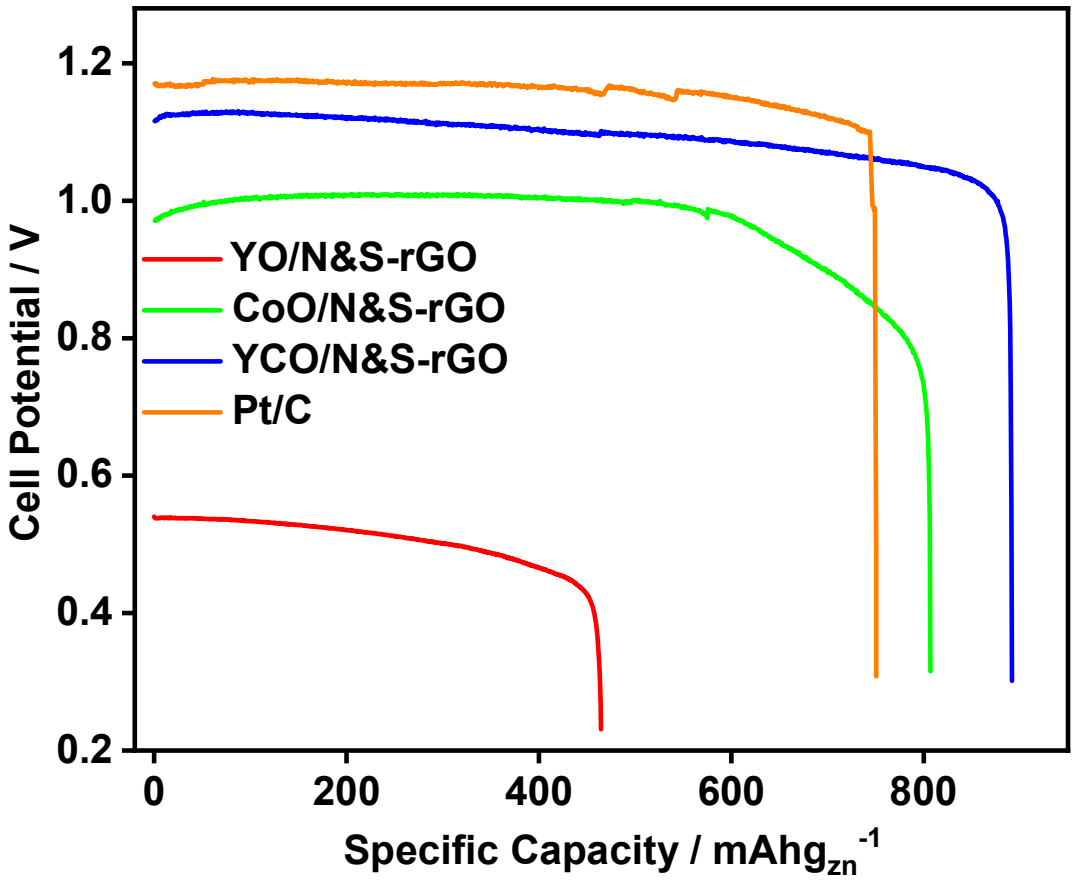

Figure S40. The specific capacity at 20 mA cm^{-2}, before accounting for the discrepancy in weight loss of Zn plate.

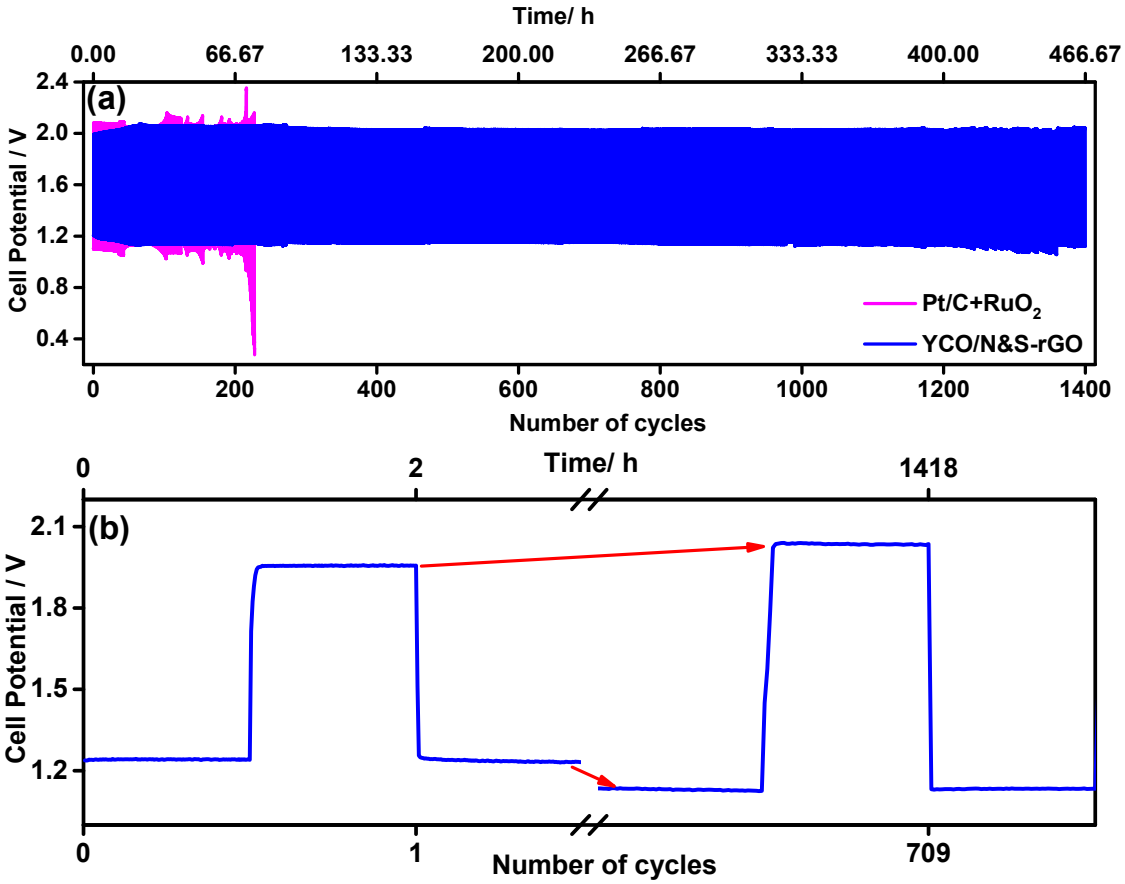

Figure S41. (a) Galvanostatic charge-discharge cycling performance of YCO/N&S-rGO and Pt/C + RuO_2 at a current density of 5 mA cm^{-2}, and (b) galvanostatic charge-discharge cycling of the YCO/N&S-rGO-based zinc-air battery under 1 h discharge and 1 h charge cycles at a current density of 5 mA cm^{-2}, showing a comparison between the first and last charge-discharge cycles.

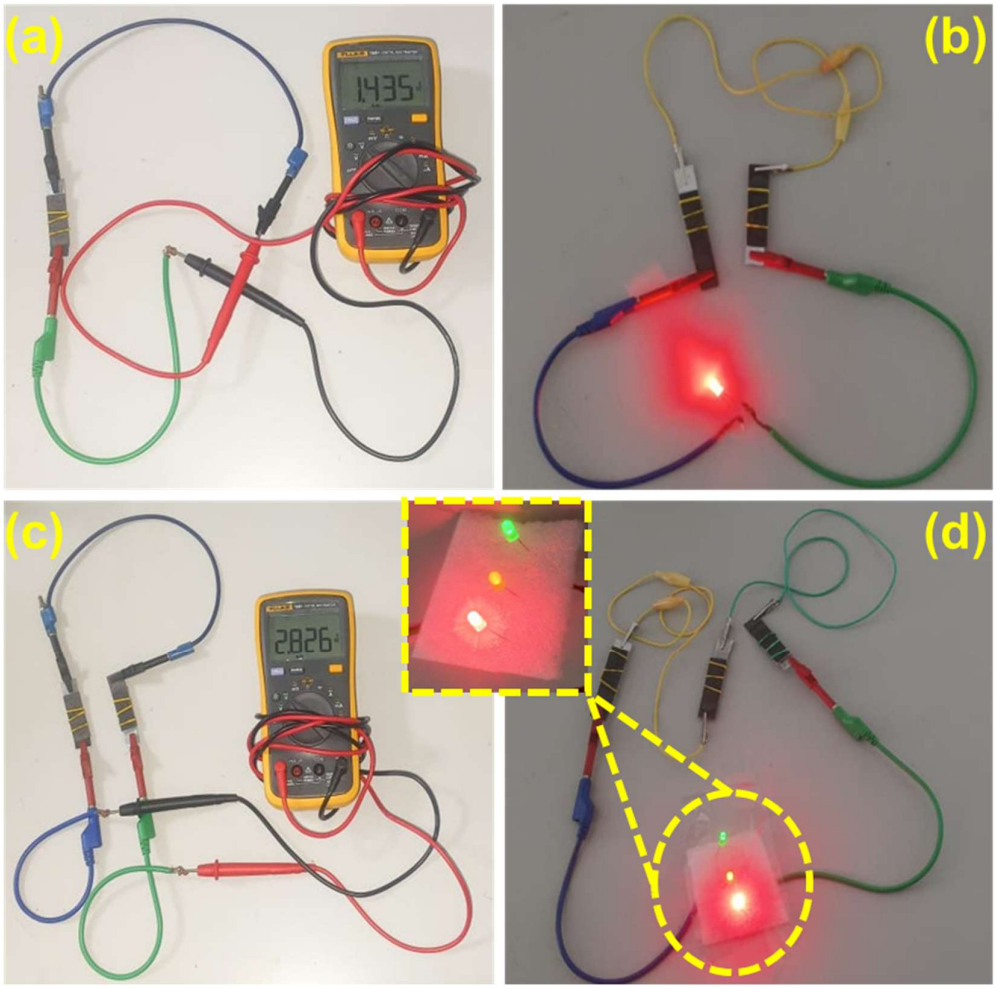

Figure S42. (a) The open circuit potentials of a solid-state ZAB with a YCO/N&S-rGO coated air electrode, and (b) the real-time application of a solid-state ZAB when it is connected with a load (in this case, an LED), (c) The open circuit potentials of two solid-state ZABs with a YCO/N&S-rGO coated air electrode connected in series and (d) the real-time application of a solid-state ZAB when it is connected with a load (in this case, three LEDs in series).

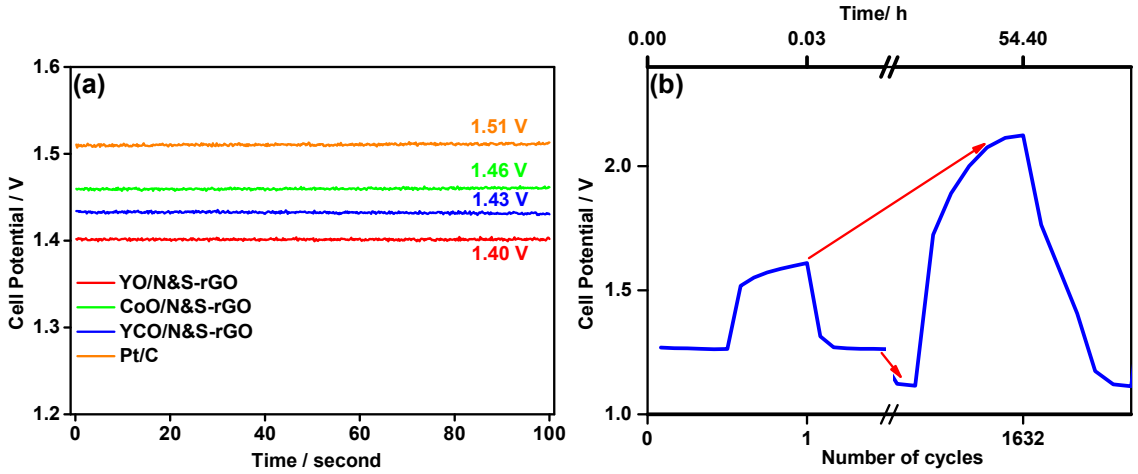

Figure S43. (a) Open-circuit potential of the solid-state zinc-air battery with the synthesized materials coated on the air electrode, and (b) galvanostatic charge-discharge cycling performance of the solid-state zinc-air battery using YCO/N&S-rGO as the air cathode catalyst under 1 minute discharge and 1 minute charge cycles at a current density of 1 mA cm^{-2}, showing a comparison between the first and last charge-discharge cycles.

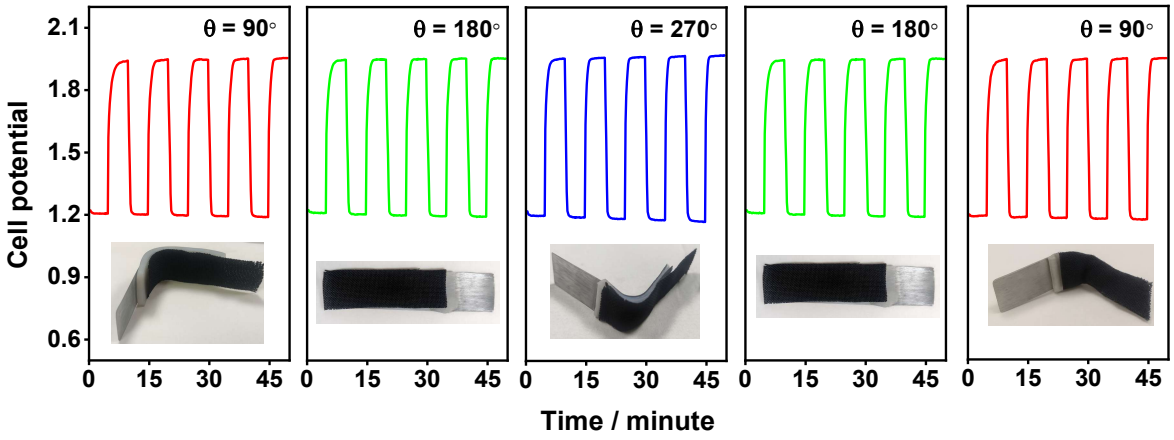

Figure S44. The charge–discharge profiles at 1 mA cm^{-2} (10 minutes per cycle) of solid-state ZAB at different angles demonstrate its flexibility.

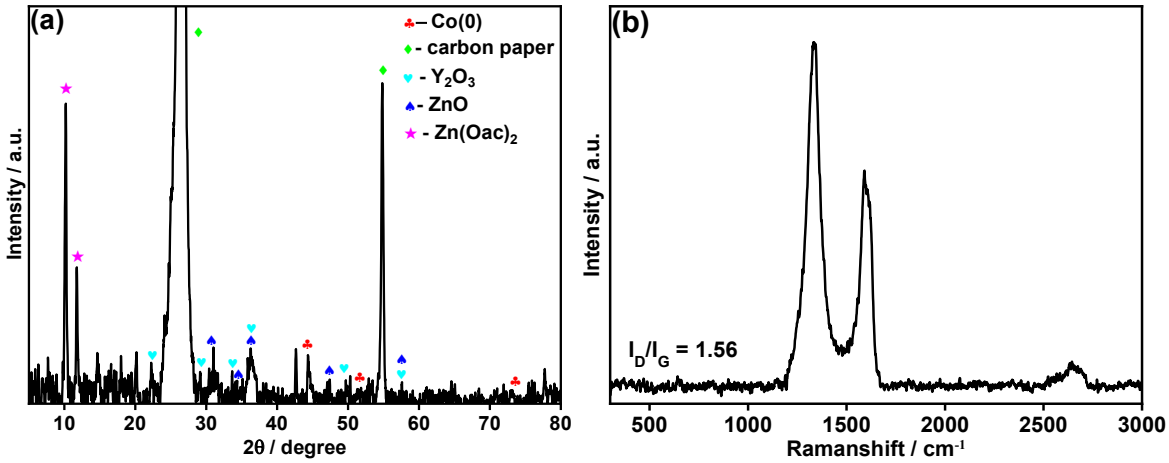

Figure S45. (a) P-XRD and (b) Raman spectra of YCO/N&S-rGO after GCD cycles.

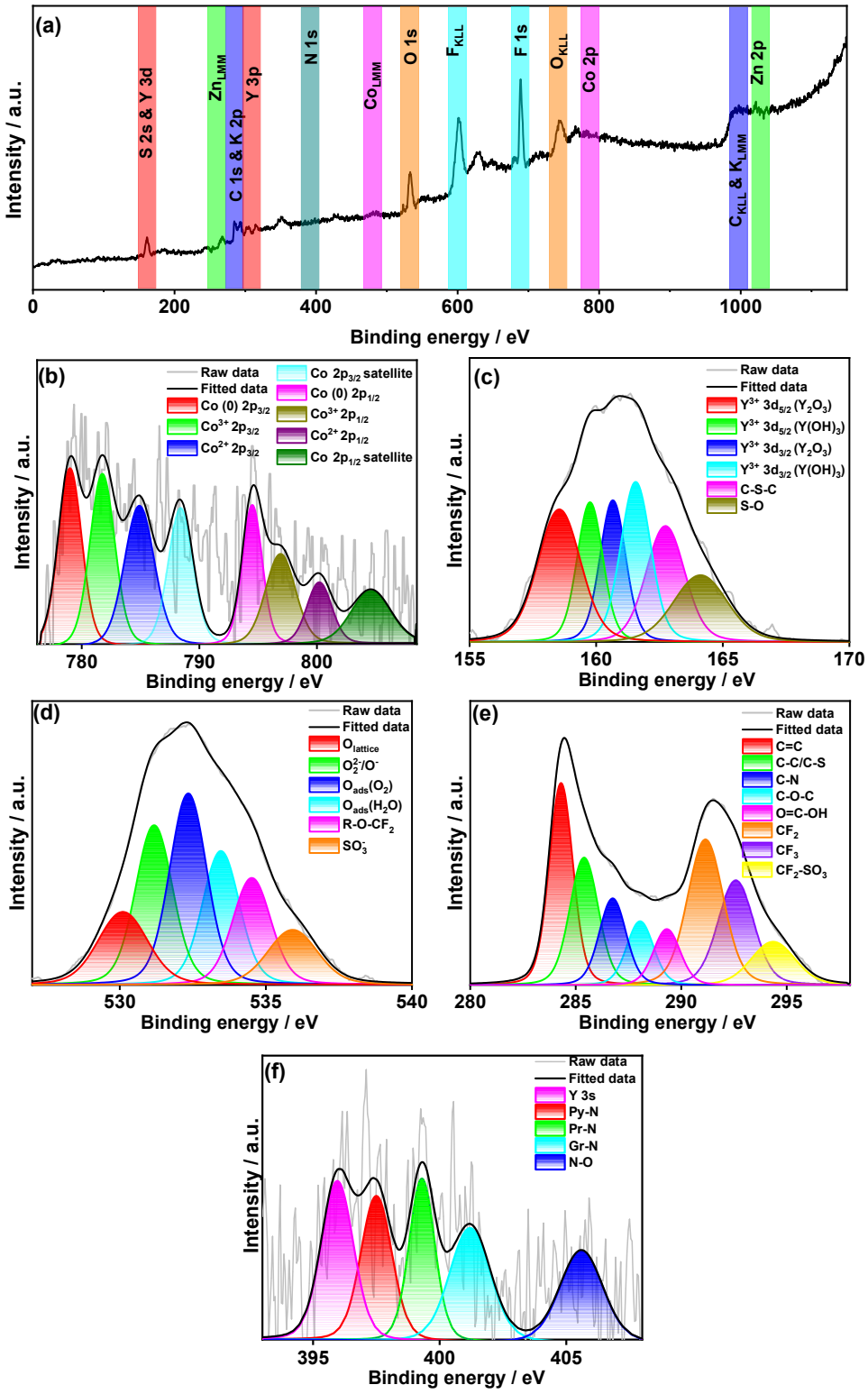

Figure S46. (a) XPS survey spectra, Core level deconvoluted spectra of (b) Co 2p, (c)Y 3d-S 2p, (d) O 1s, (e) C 1s and (f) N 1s of YCO/N&S-rGO after 700 GCD cycles (1400 hours).

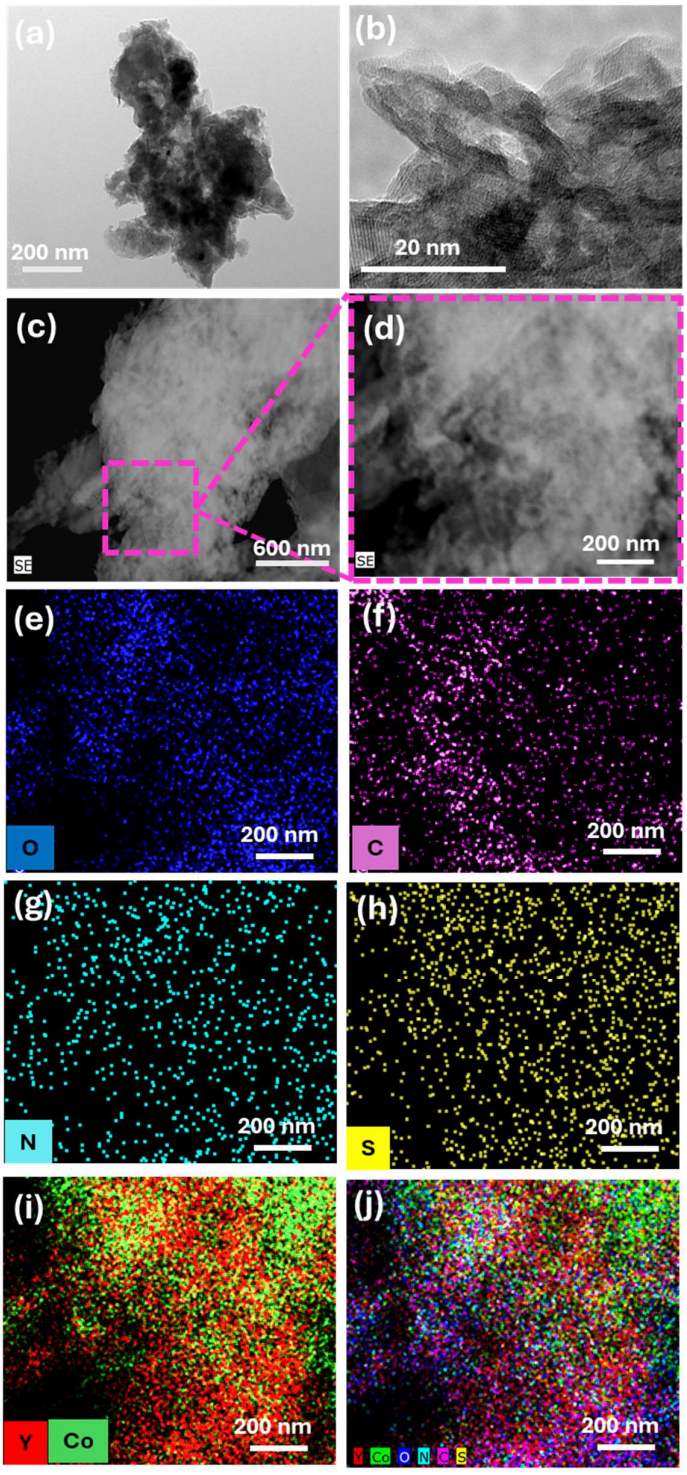

Figure S47. (a) TEM, (b) HR-TEM, (c & d) HAADF-STEM, and the corresponding EDS elemental mapping of (e) O, (f) C, (g) N, (h) S, (i) Y & Co and (j) all elements of YCO/N&S-rGO after GCD cycles.

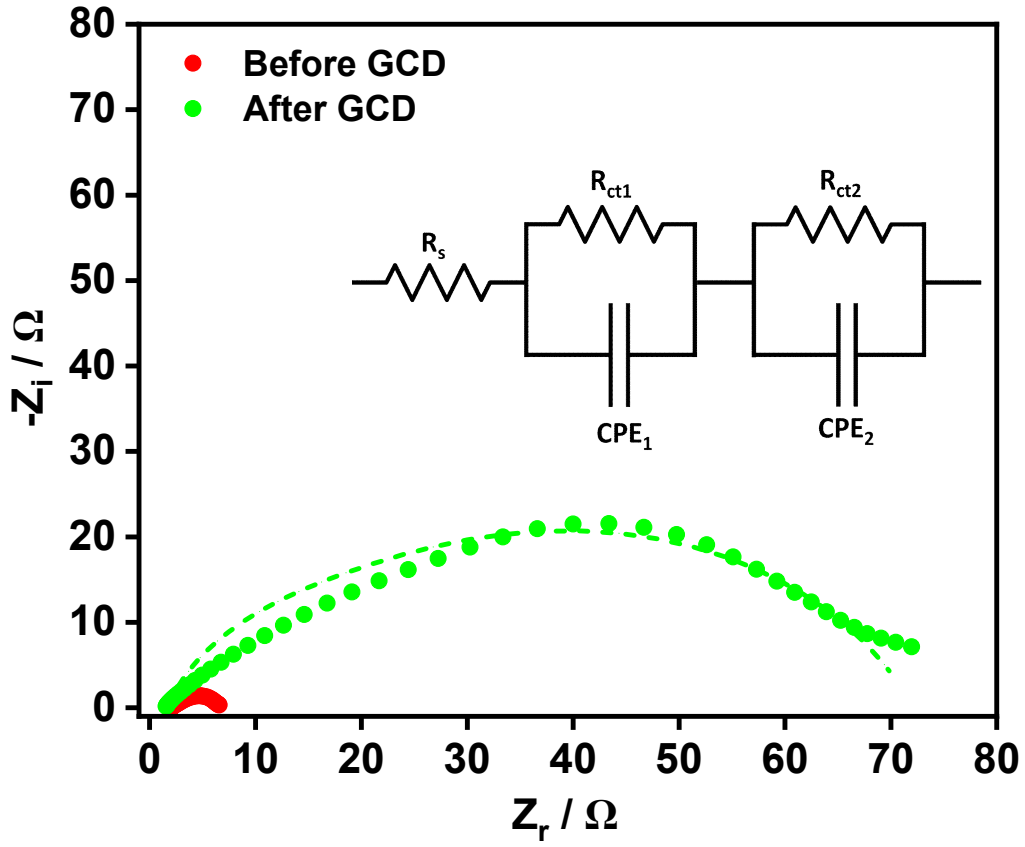

Figure S48. Electrochemical impedance spectroscopy (EIS) measured at 0.8 V in the frequency range of 10 MHz-1 mHz using an AC perturbation amplitude of 10 mV with the corresponding equivalent circuit as an inset for YCO/N&S-rGO loaded carbon paper in an aqueous electrolyte zinc-air battery configuration.

Table S1. Nomenclature of the synthesised catalysts

S. No.	Compound	Precursors	Synthesis method
1	YO	$Y(NO_3)_3.6\ H_2O$	Hydrothermal, 200 ℃, 24 h 900 ℃, 5h, air
2	CoO	$Co\ (NO_3)_2.6\ H_2O$	Hydrothermal, 200 ℃, 24 h 900 ℃, 5h, air
3	YCO	$Y(NO_3)_3.6\ H_2O$ $Co\ (NO_3)_2.6\ H_2O$ (1:1)	Hydrothermal, 200 ℃, 24 h 900 ℃, 5h, air
4	YC_2O	$Y(NO_3)_3.6\ H_2O$ $Co\ (NO_3)_2.6\ H_2O$ (1:2)	Hydrothermal, 200 ℃, 24 h 900 ℃, 5h, air
5	$Y_{1.5}CO$	$Y(NO_3)_3.6\ H_2O$ $Co\ (NO_3)_2.6\ H_2O$ (3:2)	Hydrothermal, 200 ℃, 24 h 900 ℃, 5h, air
6	$YCoO_3$	YO, CoO (1:1)	Dry ball milling 900 ℃, 5h, air
7	GO (graphene oxide)	Graphite	Modified Hummer's method
8	YO/N-rGO	YO, GO, Melamine (1:2:1)	Dry ball milling 900 ℃, 2h, N_2
9	CoO/N- rGO	CoO, GO, Melamine (1:2:1)	Dry ball milling 900 ℃, 2h, N_2
10	YCO/N- rGO	YCO, GO, Melamine (1:2:1)	Dry ball milling 900 ℃, 2h, N_2
11	YO/S-rGO	YCO, GO, Sulphur (5:10:2)	Dry ball milling 900 ℃, 2h, N_2
12	CoO/S-rGO	YCO, GO, Sulphur (5:10:2)	Dry ball milling 900 ℃, 2h, N_2
13	YCO/S-rGO	YCO, GO, Sulphur (5:10:2)	Dry ball milling 900 ℃, 2h, N_2
14	YO/N&S-rGO	YCO, GO, Melamine, Sulphur (5:10: 5:2)	Dry ball milling 900 ℃, 2h, N_2

15	CoO/N&S-rGO	YCO, GO, Melamine, Sulphur (5:10:5:2)	Dry ball milling 900 °C, 2h, N_2
16	YCO/N&S-rGO	YCO, GO, Melamine, Sulphur (5:10: 5:2)	Dry ball milling 900 °C, 2h, N_2
17	YCO/N&S-2rGO	YCO, GO, Melamine, Sulphur (5:40:10:2)	Dry ball milling 900 °C, 2h, N_2
18	N&S-rGO	GO, Melamine, Sulphur (10:5:2)	Dry ball milling 900 °C, 2h, N_2
19	[YCO+N&S-rGO]-900	YCO, N,S-rGO (1:1)	Dry ball milling 900 °C, 2h, N_2
20	2YCO/N&S-rGO	YCO, GO, Melamine, Sulphur (10:5:5:2)	Dry ball milling 900 °C, 2h, N_2
21	YCO/$N_{0.5}$&S-2rGO	YCO, GO, Melamine, Sulphur (5:40:5:2)	Dry ball milling 900 °C, 2h, N_2
22	YCO/r-GO	YCO, GO (1:2)	Dry ball milling 900 °C, 2h, N_2
23	YO-CoO/N&S-900	YO, CoO, GO, Melamine, Sulphur (5:5:20:10:4)	Dry ball milling 900 °C, 2h, N_2
24	YC_2O/N&S-rGO	YC_2O, GO, Melamine, Sulphur (5:10: 5:2)	Dry ball milling 900 °C, 2h, N_2
26	$Y_{1.5}$CO/N&S-rGO	$Y_{1.5}$CO, GO, Melamine, Sulphur (5:10: 5:2)	Dry ball milling 900 °C, 2h, N_2
27	$YCoO_3$/N&S-rGO	YCO(P), GO, Melamine, Sulphur (5:10:5:2)	Dry ball milling 900 °C, 2h, N_2
28	YCO + rGO	YCO, rGO (1:1)	Physical mixing

Table S2. Summary of parameters obtained from BET adsorption isotherms

Compound	BET S.A (m^2/g)	Pore Size (nm)	Pore volume (cm^3/g)
YCO	11.83	5.32	0.02
YO/N&S-rGO	27.19	6.98	0.05
CoO/N&S-rGO	89.00	6.18	0.14
YCO/N&S-rGO	63.78	7.64	0.12

Table S3. The ORR activity descriptors of the synthesised compounds.

S. No.	Compound	E_{onset} (V)	$E_{1/2}$ (V)	n @ j_{DL}	j_{DL} (mA/cm^2)
1	YO/N-rGO	0.93	0.78	3.4	2.72
2	CoO/N-rGO	0.92	0.83	3.5	4.01
3	YCO/N-rGO	0.93	0.81	3.5	3.40
4	YO/S-rGO	0.85	0.71	2.8	2.71
5	CoO/S-rGO	0.88	0.74	3.7	3.34
6	YCO/S-rGO	0.92	0.74	3.4	3.99
7	YO/N&S-rGO	0.98	0.76	3.1	3.09
8	CoO/N&S-rGO	0.93	0.82	3.6	3.79
9	YCO/N&S-rGO	0.97	0.85	3.6	3.95
10	YCO/rGO	0.77	0.59	3.1	1.79
11	YCO + rGO	0.90	0.78	2.6	3.10
12	N&S-rGO	0.94	0.74	2.8	2.31
13	Pt/C	1.00	0.86	3.94	5.52

Table S4. ORR activity comparison with the similar materials reported in the literature

Compound	Method	E_{onset} (V) vs. RHE	$E_{1/2}$ (V) vs. RHE	n	References
PdY/NCNT	Wet chemical method	0.98	0.865	3.9	S6
$Co_{3.2}Fe_{0.8}N$/MNC	500 °C, 2h, NH_3	0.89	0.75	-	S7
YF_3@NC	1100 °C, 3 h, Ar	0.94	0.82	3.8	S8
NiY/C@Co/C	Hydrothermal process, 150 °C, 10 h 600 °C, 4 h, N_2 900 °C, 0.5 h, N_2	0.93	0.83	3.2	S9
YN_4-Cl	900 °C, 0.5 h, N_2	0.93	0.85	3.85	S10
Y−N−C	1000 °C, 1 h, N_2	0.93	0.77	3.99	S11
Co/Ce@NC	1000 °C, Ar	0.89	0.79	3.9	S12
Pt-Y_2O_3/C	400 °C, 2 h, N_2	0.99	0.86	3.85	S13
FeY-NC	Impregnation method 950 °C, 2 h, N_2	1.02	0.93	3.93	S14
$La_{0.9}Y_{0.1}MnO_3$	Sol-gel method 700 °C, 2 h, air	0.91	0.75	3.97	S15
$FeCo_2Cr$@CN	700 °C, 2 h, N_2	0.80	0.70	~ 4	S16
YCO/N&S-rGO	**Dry ball milling, 12 h 900 °C, 2 h, N_2**	**0.97**	**0.85**	**3.6**	**This work**

Table S5. Mass-transport corrected kinetic current densities of the ORR synthesised materials

Catalysts	E_{onset} / V	$E_{1/2}$ / V	j_k (μA cm^{-2}_{ECSA})	i_k (A g^{-1})
YO/N&S-rGO	0.98	0.76	18.07	4.75
CoO/N&S-rGO	0.93	0.82	25.3	14.67
YCO/N&S-rGO	0.97	0.85	214.23	33.12
Pt/C* at 0.9 V	1.00	0.86	147.85	78.70

*ECSA of the Pt/C is calculated from hydrogen under potential deposition (HUPD)

Table S6. OER activity comparison of reported compounds from the literature.

Compound	Precursors	Synthesis Method	E_{10}^{OER} (V)	References
$Co_{3.2}Fe_{0.8}N$/MNC	$Fe(NO_3)_3 \cdot 9H_2O$ and $Co(NO_3)_2 \cdot 6H_2O$, ZIF-67-derived carbon	500 ℃, 2h, NH_3	1.67 ΔE = 0.92	S7
NiY/C@Co/C	$(Ni(NO)_2 \cdot 6H_2O)$, $(Co(NO)_2 \cdot 6H_2O)$, polyvinyl pyrrolidone, 1,3,5-Benzenetricarboxylicacid, $YCl_3 \cdot 6H_2O$, 2-methylimidazole	Hydrothermal process, 150 ℃, 10 h 600 °C, 4 h, N_2 900 °C, 0.5 h, N_2	1.62 ΔE = 0.79	S9
Fe−Co−Y oxide	$FeCl_3$, $CoCl_2$, $YCl_3 \cdot 6H_2O$, propylene oxide	Sol-gel	1.47	S12
NiYCe-MOF/NF	Naphthalenedicarboxyli acid, $Ni(Ac)_2 \cdot 4H_2O$, $Ce(NO_3)_3 \cdot 6H_2O$, $Y(NO_3)_3 \cdot 6H_2O$	Ultrasonic treatment	1.48	S16
YP-Co(OH)F	$Co(NO_3)_2 \cdot 6H_2O$, $Y(NO_3)_3 \cdot 9H_2O$, NH_4F, KOH, NaH_2PO_2	Hydrothermal process, Phosphidation 300 °C, 1 h, Ar	1.47	S17
$Y_{1.75}Co_{0.25}Ru_2O_{7-\delta}$	$Y(NO_3)_3 \cdot 6H_2O$, $Co(NO_3)_2 \cdot 6H_2O$, $RuCl_3$, citric acid, ethylene glycol	citric acid-ethylene glycol complexing method. 1100 °C, 4 h, air	1.505	S18
$Ce_{0.12}Co_{2.88}O_4$/NF	$Co(NO_3)_2$, $Ce(NO_3)_3$, urea	350 °C, 2 h, air	1.49*	S19
$Co(OH)_2$−CeO_2/Co/NF	$CoCl_2 \cdot 6H_2O$, sodium citrate, NaOH, $N_2H4 \cdot H_2O$	Hydrothermal process, 160 °C, 2 h	1.43	S20
DSA-Y-$Co(OH)_2$	$Co(NO_3)_2 \cdot 6H_2O$, $Y(NO_3)_3 \cdot 6H_2O$, Suberic acid, NaOH	Hydrothermal process, 150 °C, 12 h	1.54	S1
Co/Ce@NC.	$Zn(NO_3)_2$, $Ce(NO_3)_3 \cdot 6H_2O$, dimethylimidazole, $Co(NO_3)_2 \cdot 6H_2O$	1000 °C, Ar	1.57 ΔE = 0.78	S22

YCMO	$Y(NO_3)_3.6H_2O$, $Co(NO_3)_26H_2O$, and $Mn(acetate)_2.6H_2O$	Hydrothermal method 200 °C, 12 h 1000 °C, 4 h, air	1.82	S23
$FeCo_2Cr$@CN	$Co(acac)_2$, $Fe(acac)_3$, and Cr $(acac)_3$, toluene, melamine	700 °C, 2 h, N_2	1.544 ΔE = 0.844	S24
YCO/N&S-rGO	**$Co(NO_3)_2·6H_2O$, $Y(NO_3)_3·6H_2O$, Graphene oxide, melamine, sulphur powder**	**Dry ball milling, 12 h 900 °C, 2 h, N_2**	**1.535** ΔE = 0.69	**This work**

Table S7. Kinetic current densities for the OER of the synthesised materials (at 1.55 V vs RHE).

Catalysts	i_k (mA)	j_k (μA cm^{-2}_{ECSA})	i_k (A g^{-1})
YO/N&S-rGO	0.30	11.6	3.1
CoO/N&S-rGO	1.13	19.8	11.5
YCO/N&S-rGO	3.45	226.7	35.1
RuO_2	3.50	42.3	35.6

Table S8. The estimated OER turnover frequency for the synthesised catalysts at 1.60 V vs RHE

Catalyst	TOF (s^{-1})
YO/N&S-rGO	0.15
CoO/N&S-rGO	0.71
YCO/N&S-rGO	2.97
RuO_2	0.77

Table S9. The OER, bifunctional activities and Tafel slope of OER of the synthesised compounds.

S. No.	Compounds	E_{10} (V) of OER	$E_{1/2}$ (V) of ORR	ΔE (V)	Tafel slope (mV dec^{-1})
1	YO/N-rGO	1.94	0.78	1.16	520
2	CoO/N-rGO	1.61	0.83	0.78	114
3	YCO/N-rGO	1.63	0.81	0.82	195
4	YO/S-rGO	2.10	0.71	1.39	641
5	CoO/S-rGO	1.6	0.74	0.86	154
6	YCO/S-rGO	1.54	0.74	0.80	113
7	YO/N&S-rGO	1.73	0.76	0.97	169
8	CoO/N&S-rGO	1.57	0.82	0.75	75
9	YCO/N&S-rGO	1.54	0.85	0.69	94
10	YCO/rGO	1.60	0.59	1.01	123
11	YCO + rGO	1.68	0.78	0.90	118
12	N&S-rGO	1.68	0.74	0.94	206
13	RuO_2 & Pt/C	1.53[#]	0.86[$]	0.67*	76[#]

*ΔE calculated from the E_{10}^{OER} (RuO_2)- $E_{1/2}^{ORR}$(Pt/C)

[#] E_{10} and tafel slope of RuO_2

[$] $E_{1/2}$ of Pt/C

Table S10. The potential difference (ΔE) was determined from the difference between the potentials required to reach 10 A g^{-1} (mass-specific current density) and 10 $\mu A\ cm_{\mathrm{ECSA}}^{-2}$ (area-specific current density**)** for the OER and ORR, respectively.

Catalyst	**ΔE**		
	Conventional	**Mass specific**	**ECSA**
YO/N&S-rGO	0.97	0.92	0.69
CoO/N&S-rGO	0.75	0.73	0.69
YCO/N&S-rGO	0.69	0.65	0.44
Pt/C+RuO_2	0.67	0.53	0.50

Table S11. The HER activity descriptors of the synthesised compounds.

S. No.	Compounds	E_{10} (mV)	Tafel slope (mV dec^{-1})
1	YO/N-rGO	-0.39	-171
2	CoO/N-rGO	-0.24	-195
3	YCO/N-rGO	-0.24	-158
4	YO/S-rGO	-0.66	-214
5	CoO/S-rGO	-0.34	-159
6	YCO/S-rGO	-0.35	-179
7	YO/N&S-rGO	-0.35	-153
8	CoO/N&S-rGO	-0.26	-156
9	YCO/N&S-rGO	-0.23	-121
10	YCO/rGO	-0.58	-109
11	YCO + rGO	-0.38	-120
12	N&S-rGO	-0.55	-198
13	Pt/C	-0.05	-84

Table S12. Kinetic current densities of the HER of the synthesised materials (@-0.2 V vs. RHE)

Catalysts	i_k (mA)	j_k (μA cm^{-2}_{ECSA})	i_k(A g^{-1})
YO/N&S-rGO	0.30	11.6	3.1
CoO/N&S-rGO	0.97	17.0	9.9
YCO/N&S-rGO	1.50	98.6	15.2
Pt/C*	2.37	904.6	481.5

*Kinetic current for Pt/C calculated at 0.05 V vs. RHE.

Table S13. The HER turnover frequency was calculated for the synthesised catalysts at -0.28 V vs RHE.

Catalyst	TOF (s^{-1})
YO/N&S-rGO	0.15
CoO/N&S-rGO	0.71
YCO/N&S-rGO	2.97
Pt/C	1.69

Table S14. Co-based materials reported in the literature reported materials and their ORR< OER and HER activity comparison (all potentials referenced to RHE)

S. No.	Catalyst	$E_{1/2}$ /V	E_{10}^{OER} / V	$\Delta E = E_{10}^{OER} - E_{1/2}^{ORR}$ / V	E_{10}^{HER} / V	$\Delta E = E_{10}^{OER} - E_{10}^{HER}$ / V	Ref.
1	Co/N–CNFs	0.86	1.61	0.85	-0.24	1.85	S25
2	Co–N–C	0.84	1.58	0.74	-0.15	1.73	S26
3	FeCo–N,S-G	0.88	1.58	0.70	-0.26	1.84	S27
4	Ni_xCo_{1-x}@ $Ni_xCo_{1-x}O$/NCNT	0.79	1.61	0.82	-0.07	1.68	S28
5	Co_2P/NPG	0.81	1.55	0.74	-0.24	1.79	S29
6	Co@N-CNTF	0.81	1.58	0.77	-0.22	1.80	S30
7	Co@NC-G-700	0.83	1.55	0.72	-0.14	1.69	S31
8	Co/VN NPs@C	0.83	1.51	0.69	-0.09	1.60	S32
9	CoSA/N,S-HCS	0.85	1.58	0.73	-0.16	1.74	S33
10	NC@Co7Ni2	0.87	1.58	0.71	-0.28	1.86	S34
11	Co-CNT@NHC	0.88	1.53	0.65	-0.18	1.71	S35
12	nanoCo@bmGr-EG	0.81	1.57	0.76	-0.22	1.79	S36
13	Co_9S_8/CoNSC-900	0.89	1.57	0.68	-0.23	1.80	S37
14	Co_9S_8-HCT	0.86	1.51	0.65	-0.13	1.64	S38
15	**YCO/N&S-rGO**	**0.85**	**1.54**	**0.69**	**-0.23**	**1.77**	**This work**

Table S15. ORR and OER activity comparison of control samples by varying the heat treatment parameters

Condition	E_{onset}^{ORR} / V	E_{132} / V	E_{10}^{OER} / V	ΔE / V	*n*
Temperature					
800 °C	0.95	0.82	1.58	0.76	3.4 @ 0.4 V
900 °C	**0.97**	**0.85**	**1.54**	**0.69**	**3.7 @ 0.6 V**
950 °C	0.91	0.76	1.62	0.86	3.5 @ 0.4 V
Time					
1 hr	0.93	0.77	1.61	0.84	3.4 @ 0.4 V
2 hr	**0.97**	**0.85**	**1.54**	**0.69**	**3.7 @ 0.6 V**
4 hr	0.93	0.78	1.65	0.87	3.5 @ 0.4 V
Ramp rate					
3 °C min^{-1}	0.94	0.81	1.62	0.81	3.6 @ 0.4 V
5 °C min^{-1}	**0.97**	**0.85**	**1.54**	**0.69**	**3.7 @ 0.6 V**

Table S16. ORR and OER activity comparison of control samples by varying the precursor content.

Compound	M:C:N:S*	E_{onset}^{ORR} / V	$E_{1/2}$ / V	E_{10}^{OER} / V	ΔE / V	*n*
YCO/N&S-rGO	5:10:5:2	0.97	0.85	1.54	0.69	3.7
YCO/N&S-2rGO	5:20:10:2	0.93	0.81	1.53	0.72	3.9
YCO/N&S-4rGO	5:20:5:2	0.92	0.78	1.59	0.81	3.6
2YCO/N&S-rGO	10:5:5:2	0.9	0.75	1.64	0.89	3.8
YCO/r-GO	5:10:0:0	0.79	0.58	1.60	0.92	3.1

*Ratio between YCO (M): GO (C): Melamine (N): Sulfur powder (S)

Table S17. ORR and OER activity comparison of control samples by varying the metal content.

Compound	**M:C:N:S***	E_{onset}^{ORR} / V	$E_{1/2}$ / V	E_{10}^{OER} / V	**ΔE / V**	***n***
YCO/N&S-rGO (Y:Co= 1:1)	5:10:5:2	0.97	0.85	1.54	0.69	3.7
YC_2O/N&S-rGO (Y:Co= 1:2)	5:10:5:2	0.96	0.84	1.60	0.76	3.7
$Y_{1.5}$CO/N&S-rGO (Y:Co= 1.5:1)	5:10:5:2	0.95	0.82	1.62	0.8	3.6

*Ratio between YCO (M): GO (C): Melamine (N): Sulfur powder (S)

Table S18. Summary of liquid electrolyte ZAB performance

Compound	OCP (V)	Power density ($mW\ cm^{-2}$)	j ($mA\ cm^{-2}$)	Specific Capacity ($mA\ h\ g_{Zn}^{-1}$)	Energy density ($mW\ h\ g_{Zn}^{-1}$)
YO/N&S-rGO	1.46	10.48	16.25	446	192
CoO/N&S-rGO	1.45	26.37	48.74	688	556
YCO/N&S-rGO	1.40	89.95	129.98	778	782
Pt/C	1.54	76.05	129.99	674	738

Table S19. The recalculated specific capacity, after accounting for the discrepancy in weight of zinc consumed.

Compound	**Weight loss (g)**	**Specific Capacity (mA h g_{Zn}^{-1})**	**Corrected weight loss (g)**	**Recalculated Specific Capacity (mA h g_{Zn}^{-1})**
YO/N&S-rGO	0.1740	454	0.1773	446
CoO/N&S-rGO	0.3523	789	0.4039	688
YCO/N&S-rGO	0.4298	877	0.4847	778
Pt/C	0.4831	744	0.5336	674

Table S20. Comparison ZAB performance of synthesised materials with the literature

Compounds	OCP (V)	Power density (mW cm^{-2}) @ current density (mA cm^{-2})	Specific Capacity (mA h g_{Zn}^{-1}) @ current density (mA cm^{-2})	Cycling stability (h) @ current density (mA cm^{-2})	Ref.
PdY/NCNT	-	236 @ 420	700.58 @ 10	-	S6
YF_3@NC	1.48	75 @ 124	620 @ 10	-	S7
NiY/C@Co/C	1.39	102.2 @ 170	899.6 @ 5	-	S9
YN_4-Cl	-	162 @ 277	770 @ 200 mA	20 @ 20	S10
Co/Ce@NC	1.45	206 @ 329.2	798 @ 5	450 @ 5	S12
FeY-NC	1.48	233 @ 325	772 @ 200	25 @ 20	S14
$La_{0.9}Y_{0.1}MnO_3$	-	167.4 @ 225	-	-	S15
$FeCo_2Cr$@CN	1.36	121.6 @ 209.6	-	100 @ 5	S16
Co-NTMCs@NSC	1.51	262 @ 350	800 @ 10	12 @ 10	S39
Co/CeO_2–NCNA@CC	1.47	123 @ 217	784.4 @ 5	40 @ 5	S40
NCO/CO-500	1.34	-	-	120 @ 10	S41
Co_3O_4/CoNGDY	1.50	128	746.8	5000 @ 2 1667 @10	S42
Co@NC-800	1.44	244.16	721.67	420 @ 5	S43
FeCoOx/Fe─N─C	-	184.8 @ 300	811.8 @ 10	30 @ 5	S44
CMMCO	1.50	179 @ 315	779.8 @ 10	490 @ 10	S45
FeCo/Fe-CoS/NSC	1.63	164.7 @ 210.01	793 @ 10	120 @ 10	S46
NCO/CO-500	1.34	-	-	120 @ 10	S41
Co_3O_4/CoNGDY	1.50	128	746.8	5000 @ 2 1667 @10	S42
Co@NC-800	1.44	244.16	721.67	420 @ 5	S43
FeCoOx/Fe─N─C	-	184.8 @ 300	811.8 @ 10	30 @ 5	S44
CMMCO	1.50	179 @ 315	779.8 @ 10	490 @ 10	S45

FeCo/Fe-CoS/NSC	1.63	164.7 @ 210.01	793 @ 10	120 @ 10	S46
CoSn@NC	1.44	282 @ 463	817 @ 10	99 @ 10	S47
CoL 2:1	-	161 @ 320	804 @ 5	200 @ 10	S48
Co/N–CNF-800	-	-	-	50 @ 10	S49
Co/Co_3O_4@NC	1.57	156.5 @ 200	809.6 @ 10	220 @ 10	S50
Co-NC500	1.51	150.6 @ 190.6	-	136 @ 5	S51
Cu Co NHCS	1.61	176 @ 376	781 @ 5	200 @ 5	S52
(Y1La1)O/Co-NC	1.44	-	955.73 @ 10	128 @ 10	S53
YCO/N&S-rGO	**1.40**	**90 @ 130**	**877 @ 20**	**1420 @ 5**	**This work**

Table S21. Summary of solid-state zinc air battery performance.

Compound	OCP (V)	Power density (mW cm^{-2})	Current density (mA cm^{-2})
YO/N&S-rGO	1.40	6.7	11.7
CoO/N&S-rGO	1.46	14.4	23.3
YCO/N&S-rGO	1.43	21.75	33.65
Pt/C	1.51	20.5	28.3

Table S22. The fitted parameters for the equivalent circuit of Nyquist plots measured at 0.8 V in the frequency range of 10 kHz–10 mHz using an AC perturbation amplitude of 10 mV for of YCO/N&S-rGO loaded carbon paper in an aqueous electrolyte zinc–air battery configuration before and GCD cycling.

	R_s (Ω)	R_{ct1} (Ω)	CPE_1 ($Ω^{-1}$ S^{n1})	n_1	R_{ct2} (Ω)	CPE_2 ($Ω^{-1}$ S^{n2})	n_2	χ^2
Before	2.09	2.55	0.10	0.69	4.41	0.05	0.80	2.106e-04
After	1.68	12.38	0.006	0.8	58.08	0.009	0.08	2.118e-02

References

(S1) Roy, A.; Kang, K.-M.; Nah, Y.-C.; La, M.; Choi, D.; Park, S. J. Improved Electrocatalytic Water Oxidation with Cobalt Hydroxide Nano-Flakes Supported on Copper-Modified Nickel Foam. *Electrochim Acta* **2021**, *383*, 138368.

(S2) Browne, M. P.; Nolan, H.; Duesberg, G. S.; Colavita, P. E.; Lyons, M. E. G. Low-Overpotential High-Activity Mixed Manganese and Ruthenium Oxide Electrocatalysts for Oxygen Evolution Reaction in Alkaline Media. *ACS Catal* **2016**, *6* (4), 2408–2415.

(S3) Sadhukhan, A.; Karmakar, A.; Koner, K.; Karak, S.; Sharma, R. K.; Roy, A.; Sen, P.; Dey, K. K.; Mahalingam, V.; Pathak, B.; et al. Functionality Modulation Toward Thianthrene-based Metal-Free Electrocatalysts for Water Splitting. *Advanced Materials* **2024**, *36* (18), 2310938.

(S4) Paulchamy, B.; Arthi, G.; Lignesh, B. D. A Simple Approach to Stepwise Synthesis of Graphene Oxide Nanomaterial, *J. Nanomed. Nanotechnol* **2015**, *6* (1), 1.

(S5) Eledath, A. N.; Edathiparambil Poulose, A.; Muthukrishnan, A. Origin of the Oxygen Reduction Activity on Boron-Doped Fe–N–C Catalysts for Zinc–Air Battery Applications. *ACS Appl. Energy Mater.* **2024**, *7* (6), 2378–2391.

(S6) Roy, N.; Ahmed, M. S.; Lee, H. K.; Jeon, S. Intermetallic Pd–Y nanoparticles/N-doped carbon nanotubes as multi-active catalysts for oxygen reduction reaction, ethanol oxidation reaction, and zinc–air batteries. *Nanoscale* **2024**, *16* (15), 7532-7546.

(S7) Zhang, K.; Mai, W.; Li, J.; Li, G.; Tian, L.; Hu, W. Bimetallic Co3.2Fe0.8N–Nitrogen–Carbon Nanocomposites for Simultaneous Electrocatalytic Oxygen Reduction, Oxygen Evolution, and Hydrogen Evolution. *ACS Applied Nano Materials* **2019**, *2* (9), 5931-5941.

(S8) Wang, W.; Mi, Y.; Kang, Y.; Liu, X.; Imhanria, S.; Lei, Z. Yttrium fluoride doped nitrogen-contained carbon as an efficient cathode catalyst in zinc-air battery. *Journal of Power Sources* **2020**, *472*, 228451.

(S9) Liu, F.; Peng, H.; Kang, Y.; Hao, Y.; Li, L.; Xin, H.; Kang, H.; Wang, W.; Lei, Z. Rare-Earth-Based Bimetallic Metal–Organic Frameworks Promote Oxygen Electrocatalysis for Rechargeable Zn–Air Batteries. *ACS Sustainable Chemistry & Engineering* **2022**, *10* (33), 10978-10988.

(S10) Ji, B.; Gou, J.; Zheng, Y.; Pu, X.; Wang, Y.; Kidkhunthod, P.; Tang, Y. Coordination Chemistry of Large-Sized Yttrium Single-Atom Catalysts for Oxygen Reduction Reaction. *Advanced Materials* **2023**, *35* (24), 2300381.

(S11) Parida, S. K.; Chalke, B. A.; Kaur, G.; Yadav, A. K.; Jena, H. A Metal–Organic Framework-Derived Atomically Dispersed Yttrium as an Electrocatalyst for Oxygen Reduction Reaction. *ACS Applied Energy Materials* **2024**, *7* (4), 1583-1589.

(S12) Wu, K.; Wang, D.; Fu, Q.; Xu, T.; Xiong, Q.; Peera, S. G.; Liu, C. Co/Ce-MOF-Derived Oxygen Electrode Bifunctional Catalyst for Rechargeable Zinc–Air Batteries. *Inorganic Chemistry* **2024**, *63* (24), 11135-11145.

(S13) Luo, Y.; Habrioux, A.; Calvillo, L.; Granozzi, G.; Alonso-Vante, N. Yttrium Oxide/Gadolinium Oxide-Modified Platinum Nanoparticles as Cathodes for the Oxygen Reduction Reaction. *ChemPhysChem* **2014**, *15* (10), 2136-2144.

(S14) Luo, R.; Wang, R.; Cheng, Y.; Meng, Z.; Wang, Y.; Guo, Z.; Xu, B. B.; Xia, Y.; Tang, H. Yttrium Oxide Nanoclusters Boosted Fe-N4 and Fe4N Electrocatalyst for Future Zinc–Air Battery. *Advanced Functional Materials* **2024**, *34* (11), 2311084.

(S15) Miao, H.; Wang, Z.; Wang, Q.; Sun, S.; Xue, Y.; Wang, F.; Zhao, J.; Liu, Z.; Yuan, J. A new family of Mn-based perovskite ($La_{1-x}Y_xMnO_3$) with improved oxygen electrocatalytic activity for metal-air batteries. *Energy* **2018**, *154*, 561-570.

(S16) Kumar, R.; Kumar, S.; Chandrappa, S. G.; Goyal, N.; Yadav, A.; Ravishankar, N.; Prakash, A. S.; Sahoo, B. Nitrogen-doped carbon nanostructures embedded with Fe-Co-Cr alloy based nanoparticles as robust electrocatalysts for Zn-air batteries. *Journal of Alloys and Compounds* **2024**, *984*, 173862.

(S17) Zhang, Q.; Liu, N.; Guan, J. Charge-Transfer Effects in Fe–Co and Fe–Co–Y Oxides for Electrocatalytic Water Oxidation Reaction. *ACS Applied Energy Materials* **2019**, *2* (12), 8903-8911. DOI: 10.1021/acsaem.9b01938.

(S18) Li, F.; Jiang, M.; Lai, C.; Xu, H.; Zhang, K.; Jin, Z. Yttrium- and Cerium-Codoped Ultrathin Metal–Organic Framework Nanosheet Arrays for High-Efficiency Electrocatalytic Overall Water Splitting. *Nano Letters* **2022**, *22* (17), 7238-7245.

(S19) Zhang, G.; Wang, B.; Li, L.; Yang, S. Phosphorus and Yttrium Codoped Co(OH)F Nanoarray as Highly Efficient and Bifunctional Electrocatalysts for Overall Water Splitting. *Small* **2019**, *15* (42), 1904105.

(S20) Han, N.; Feng, S.; Liang, Y.; Wang, J.; Zhang, W.; Guo, X.; Ma, Q.; Liu, Q.; Guo, W.; Zhou, Z.; et al. Achieving Efficient Electrocatalytic Oxygen Evolution in Acidic Media on

Yttrium Ruthenate Pyrochlore through Cobalt Incorporation. *Advanced Functional Materials* **2023**, *33* (20), 2208399.

(S21) Du, Y.; Tang, H.; Zhang, D.; Liu, H.; Chen, Y.; Zhu, Z.; Yang, W.; Li, Z.; Tang, Y.; Liu, C. Boosting Electrocatalytic Oxygen Evolution: Superhydrophilic/Superaerophobic Hierarchical Nanoneedle/Microflower Arrays of $Ce_xCo_{3-x}O_4$ with Oxygen Vacancies. *ACS Applied Materials & Interfaces* **2021**, *13* (36), 42843-42851.

(S22) Li, T.; Gu, F.; Chen, X. H.; Zhang, Q.; Fu, H. C.; Luo, H. Q.; Li, N. B. Engineered Superhydrophilic/Superaerophobic Catalyst: Two-Dimensional $Co(OH)_2$–CeO_2 Nanosheets Supported on Three-Dimensional Co Dendrites for Overall Water Splitting. *Inorganic Chemistry* **2023**, *62* (6), 2784-2792.

(S23) Jing, H.; Zhao, P.; Yu, J.; Wu, Z.; Liu, B.; Lei, W.; Hao, Q. Suberic Acid-Modified Y-$Co(OH)_2$ Nanosheets with Cationic Vacancies for Efficient Oxygen Evolution Reaction. *ACS Sustainable Chemistry & Engineering* **2023**, *11* (14), 5428-5439.

(S24) McGuire, S. C.; Wesley, W.; Sasaki, K.; Tong, X.; Wong, S. S. Yttrium-based Double Perovskite Nanorods for Electrocatalysis. *ACS Applied Materials & Interfaces* **2022**, *14* (27), 30914-30926.

(S25) Liu, J.; Zhou, J.; Leung, M. K. H. Valence Engineering of Polyvalent Cobalt Encapsulated in a Carbon Nanofiber as an Efficient Trifunctional Electrocatalyst for the Zn–Air Battery and Overall Water Splitting. *ACS Appl Mater Interfaces* 2022, *14* (3), 4399–4408.

(S26) Deng, C.; Wu, K.-H.; Scott, J.; Zhu, S.; Zheng, X.; Amal, R.; Wang, D.-W. Spherical Murray-Type Assembly of Co–N–C Nanoparticles as a High-Performance Trifunctional Electrocatalyst. *ACS Appl Mater Interfaces* 2019, *11* (10), 9925–9933.

(S27)Liu, Y.; Duan, W.; Pei, H.; Sun, P.; Sun, Y.; Zhuang, Y.; Li, Z. Multi-Level Porous Fe, Co, N, S Co-Doped Three-Dimensional Graphene-like Catalyst as the Excellent Trifunctional Electrocatalyst for Liquid and Flexible All-Solid-State Zinc–Air Batteries. *ACS Appl Energy Mater* 2023, *6* (13), 7194–7204.

(S28) Jena, R.; Bhattacharyya, S.; Bothra, N.; Kashyap, V.; Pati, S. K.; Maji, T. K. NixCo1–X@NixCo1–XO/NCNT as Trifunctional ORR, OER, and HER Electrocatalysts and Its Application in a Zn–Air Battery. *ACS Appl Mater Interfaces* 2023, *15* (23), 27893–27904.

(S29) Shao, Q.; Li, Y.; Cui, X.; Li, T.; Wang, H.; Li, Y.; Duan, Q.; Si, Z. Metallophthalocyanine-Based Polymer-Derived Co2P Nanoparticles Anchoring on Doped Graphene as High-Efficient Trifunctional Electrocatalyst for Zn-Air Batteries and Water Splitting. *ACS Sustain Chem Eng* 2020, *8* (16), 6422–6432.

(S30) Guo, H.; Feng, Q.; Zhu, J.; Xu, J.; Li, Q.; Liu, S.; Xu, K.; Zhang, C.; Liu, T. Cobalt Nanoparticle-Embedded Nitrogen-Doped Carbon/Carbon Nanotube Frameworks Derived from a Metal–Organic Framework for Tri-Functional ORR, OER and HER Electrocatalysis. *J Mater Chem A Mater* 2019, *7* (8), 3664–3672.

(S31) Wen, X.; Yang, X.; Li, M.; Bai, L.; Guan, J. Co/CoOx Nanoparticles Inlaid onto Nitrogen-Doped Carbon-Graphene as a Trifunctional Electrocatalyst. *Electrochim Acta* 2019, *296*, 830–841.

(S32) Zheng, H.; Xu, N.; Hou, B.; Zhao, X.; Dong, M.; Sun, C.; Wang, X.-L.; Su, Z.-M. Bimetallic Metal–Organic Framework-Derived Graphitic Carbon-Coated Small Co/VN Nanoparticles as Advanced Trifunctional Electrocatalysts. *ACS Appl Mater Interfaces* 2021, *13* (2), 2462–2471.

(S33) Zhang, Z.; Zhao, X.; Xi, S.; Zhang, L.; Chen, Z.; Zeng, Z.; Huang, M.; Yang, H.; Liu, B.; Pennycook, S. J.; Chen, P. Atomically Dispersed Cobalt Trifunctional Electrocatalysts with Tailored Coordination Environment for Flexible Rechargeable Zn–Air Battery and Self-Driven Water Splitting. *Adv Energy Mater* 2020, *10* (48), 2002896..

(S34) Han, C.; Li, H.; Pan, A.; Dou, S.; Liu, Y.; Liu, J.; Li, W. Tri-Functional Carbon Nanocages Coated CoNi Electrocatalyst with Micro Twinning Structure for High-Performance Electrochemical Devices. *Chemical Engineering Journal* 2024, *481*, 148073.

(S35) Zhuang, Y.; Cheng, H.; Meng, C.; Chen, B.; Zhou, H. Self-Catalyzed Co, N-Doped Carbon Nanotubes-Grafted Hollow Carbon Polyhedrons as Efficient Trifunctional Electrocatalysts for Zinc-Air Batteries and Self-Powered Overall Water Splitting. *J Colloid Interface Sci* 2023, *643*, 162–173.

(S36) Fan, W.; Tang, X.; Yi, Q.; Li, G. Nitrogen-Doped Graphite Supported Cobalt Nanoparticles as Excellent ORR/OER/HER Trifunctional Electrocatalysts. *Fuel* 2025, *397*, 135382.

(S37) Zhang, J.; Cui, B.; Jiang, S.; Liu, H.; Dou, M. Construction of Three-Dimensional Cobalt Sulfide/Multi-Heteroatom Co-Doped Porous Carbon as an Efficient Trifunctional Electrocatalyst. *Nanoscale* 2022, *14* (27), 9849–9859.

(S38) Zhao, J.; Zhou, J.; Zhang, Z.; Li, Q.; Liu, R. Hierarchical Assembly Strategy to Tailored Nanostructures of Doped-Carbon/Co-Based Catalysts for High-Performance Trifunctional Electrocatalysis. *Chemical Engineering Journal* 2021, *418*, 129365.

(S39) Zhu, X.; Dai, J.; Li, L.; Wu, Z.; Chen, S. N,S–Codoped hierarchical porous carbon spheres embedded with cobalt nanoparticles as efficient bifunctional oxygen electrocatalysts for rechargeable zinc-air batteries. *Nanoscale* **2019**, *11* (44), 21302-21310.

(S40) Li, S.; Zhang, H.; Wu, L.; Zhao, H.; Li, L.; Sun, C.; An, B. Vacancy-engineered CeO2/Co heterostructure anchored on the nitrogen-doped porous carbon nanosheet arrays vertically grown on carbon cloth as an integrated cathode for the oxygen reduction reaction of rechargeable Zn–air battery. *Journal of Materials Chemistry A* **2022**, *10* (18), 9858-9868.

(S41) Ayyaluri, R. R.; Ankinapalli, O. R.; Yu, J. S. Trifunctional Catalytic Properties of Nickel Cobalt Oxide/Cobalt Oxide Electrocatalysts for Rechargeable Zinc-Air Battery and Water Splitting Applications. *Int J Hydrogen Energy* **2025**, *148*, 150048. https://doi.org/https://doi.org/10.1016/j.ijhydene.2025.150048.

(S42) Chang, Q.; He, F.; Zhang, Z.; Fu, X.; Wang, Y.; Huang, C.; Li, Y. Self-Organized Integrated Electrocatalyst on Oxygen Conversion for Highly Durable Zinc-Air Batteries. *Angewandte Chemie International Edition* **2025**, *64* (4), e202416664.

(S43) Ren, Y.-T.; Yuan, Y.-Y.; Xiang, Y.; Zhao, H.; Hao, H.-G.; Ma, H.-Y.; Wang, S.-N.; Li, Y.-W. Coupling of Metallic Co with Atomic Co–N–C as Efficient Bifunctional Oxygen Electrocatalyst for Rechargeable Zinc-Air Battery. *J Alloys Compd* **2025**, *1044*, 184447.

(S44) Wei, K.; Yang, F.; Sun, Y.; Yu, C.; An, J.; Ma, G.; Li, Y. Tailoring Oxygen Electrocatalytic Performance via Construction of Iron-Cobalt Oxides and FeN4 Sites on Hierarchical Carbon Fibers for Efficient Zinc–Air Batteries. *Adv Funct Mater* **2025**, *35* (32), 2422039.

(S45) Sun, B.; Liu, P.; Wang, P.; Wang, M.; Chai, Y.; Cui, F.; Jin, Y. Efficient Construction of Heterogeneous Oxides as Robust Bifunctional Electrocatalysts for Zinc-Air Batteries. *Small* **2025**, *21* (30), 2501938.

(S46) Ko, D.; Min, K.; Lee, B.; Kwon, H.; Baeck, S.-H. Highly Efficient Bifunctional Electrocatalyst for Rechargeable Zinc-Air Batteries: N, S Dual-Doped Carbon Encapsulating Sulfur Vacancy-Rich FeCo/Fe-CoS Nanoparticles. *J Power Sources* **2025**, *625*, 235653.

(S47) Ghora, S.; Raj, C. R. Shape-Controlled Synthesis of Nitrogen-Doped Carbon Encapsulated CoSn Intermetallic Electrocatalyst for Neutral and Alkaline Zinc–Air Batteries. *ACS Appl Mater Interfaces* **2025**, *17* (44), 60490–60501.

(S48) Allwyn, N.; Gokulnath, S.; Sathish, M. In-Situ Nanoarchitectonics of Fe/Co LDH over Cobalt-Enriched N-Doped Carbon Cookies as Facile Oxygen Redox Electrocatalysts for High-

Rate Rechargeable Zinc–Air Batteries. *ACS Appl Mater Interfaces* **2024**, *16* (16), 20360–20374.

(S49) Liu, J.; Zhou, J.; Leung, M. K. H. Valence Engineering of Polyvalent Cobalt Encapsulated in a Carbon Nanofiber as an Efficient Trifunctional Electrocatalyst for the Zn–Air Battery and Overall Water Splitting. *ACS Appl Mater Interfaces* **2022**, *14* (3), 4399–4408.

(S50) Xu, H.-M.; Zhu, H.-R.; Zhang, Z.-J.; Huang, C.-J.; Shuai, T.-Y.; Zhan, Q.-N.; Li, G.-R. Co/Co3O4 Heterojunctions Encased in Porous N-Doped Carbon Nanocapsules for High-Performance Cathode of Rechargeable Zinc–Air Batteries. *Inorg Chem* **2024**, *63* (8), 3702–3711.

(S51) Kumar, S.; Kumar, R.; Goyal, N.; Vazhayil, A.; Yadav, A.; Thomas, N.; Sahoo, B. N-Doped Carbon Nanotubes Nucleated through Cobalt Nanoparticles as Bifunctional Catalysts for Zinc–Air Batteries. *ACS Appl Nano Mater* **2024**, *7* (7), 7865–7882.

(S52) Somasundharam, H. P.; Allwyn, N.; Sathish, M.; Senthil Kumar, S. M. Synergizing Energy Storage: Copper Cobalt Oxide Integrated Nitrogen-Doped Carbon Spheres for Advanced Zinc–Air Batteries. *ACS Appl Energy Mater* **2025**, *8* (15), 11688–11705.

(S53) Liu, F.; Lu, X.; Shi, C.; Wang, D.; Cui, T.; Sun, Z. Y2O3/La2O3 Electron Modulation Engineering of Co Site for Boosting Oxygen Electrocatalysis. *Chemical Engineering Journal* **2025**, *524*, 169780.